

AD-A268 530



WL-TR-93-2087

CARS TEMPERATURE MEASUREMENTS AND  
STABILITY STUDIES OF A D.C. NITROGEN  
DISCHARGE

Michael Millard

UNIVERSITY OF DAYTON  
School of Engineering  
Dayton, OH

July 1991



DTIC  
ELECTE  
AUG 20 1993  
S B D

Final Report for Period September 1989 - July 1991

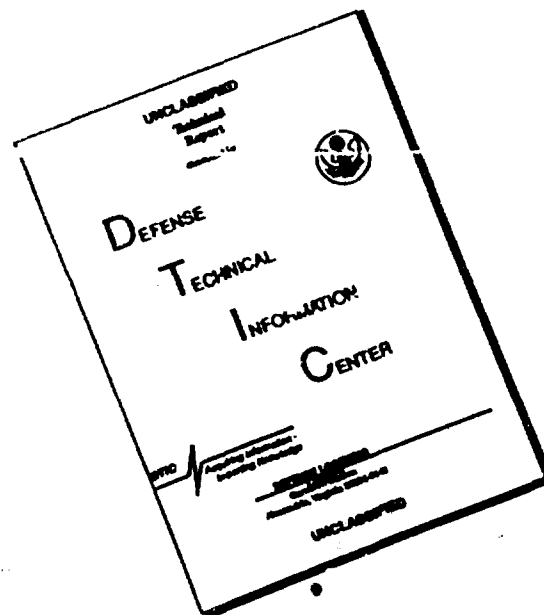
Approved for public release; distribution unlimited.

AERO PROPULSION AND POWER DIRECTORATE  
WRIGHT LABORATORY  
AIR FORCE SYSTEMS COMMAND  
WRIGHT-PATTERSON AIR FORCE BASE, OH 45433-6563

93 8 19 023

93-19313

# DISCLAIMER NOTICE



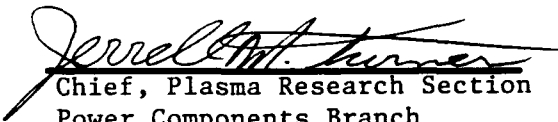
THIS DOCUMENT IS BEST  
QUALITY AVAILABLE. THE COPY  
FURNISHED TO DTIC CONTAINED  
A SIGNIFICANT NUMBER OF  
PAGES WHICH DO NOT  
REPRODUCE LEGIBLY.


## NOTICE


WHEN GOVERNMENT DRAWINGS, SPECIFICATIONS, OR OTHER DATA ARE USED FOR ANY PURPOSE OTHER THAN IN CONNECTION WITH A DEFINITELY GOVERNMENT-RELATED PROCUREMENT, THE UNITED STATES GOVERNMENT INCURS NO RESPONSIBILITY OR ANY OBLIGATION WHATSOEVER. THE FACT THAT THE GOVERNMENT MAY HAVE FORMULATED OR IN ANY WAY SUPPLIED THE SAID DRAWINGS, SPECIFICATIONS, OR OTHER DATA, IS NOT TO BE REGARDED BY IMPLICATION, OR OTHERWISE IN ANY MANNER CONSTRUED, AS LICENSING THE HOLDER, OR ANY OTHER PERSON OR CORPORATION; OR AS CONVEYING ANY RIGHTS OR PERMISSION TO MANUFACTURE, USE, OR SELL ANY PATENTED INVENTION THAT MAY IN ANY WAY BE RELATED THERETO.

This report is releasable to the National Technical Information Service (NTIS). At NTIS, it will be available to the general public, including foreign nations.

THIS TECHNICAL REPORT HAS BEEN REVIEWED AND IS APPROVED FOR PUBLICATION.

  
Chief, Plasma Research Section  
Power Components Branch  
Aerospace Power Division  
Aero Propulsion and Power Directorate

  
Act Branch Chief, Power Components Branch  
Aerospace Power Division  
Aero Propulsion and Power Directorate

  
BRAYDICH, MICHAEL D., Lt Col USAF  
Deputy Chief  
Aerospace Power Division  
Aero Propulsion and Power Directorate

DTIC QUALITY INSPECTED 3

IF YOUR ADDRESS HAS CHANGED, IF YOU WISH TO BE REMOVED FROM OUR MAILING LIST, OR IF THE ADDRESSEE IS NO LONGER EMPLOYED BY YOUR ORGANIZATION PLEASE NOTIFY WL/POOC, WRIGHT-PATTERSON AFB, OH 45433-6553 TO HELP MAINTAIN A CURRENT MAILING LIST.

COPIES OF THIS REPORT SHOULD NOT BE RETURNED UNLESS RETURN IS REQUIRED BY SECURITY CONSIDERATIONS, CONTRACTUAL OBLIGATIONS, OR NOTICE ON A SPECIFIC DOCUMENT.

or	
<input checked="checked" type="checkbox"/>	<input type="checkbox"/>
<input type="checkbox"/>	<input type="checkbox"/>
on	
Codes	
Dist	and/or Special
A-1	

July 1991

Final Sept 89 - Jul 91

**CARS TEMPERATURE MEASUREMENTS AND STABILITY STUDIES  
OF A D.C. NITROGEN DISCHARGE**

C F33615-81-C-2012  
PE 61102F  
PR 2301  
TA S1  
WU 18

Michael Millard

University of Dayton  
School of Engineering  
Dayton, OH 45469

Aero Propulsion and Power Directorate  
Wright Laboratory  
Air Force Systems Command  
Wright-Patterson Air Force Base, OH 45433-6553

WL-TR-93-2087

Approved for public release; distribution unlimited

Vibrational and rotational temperatures of a 30-Torr, normal glow  $N_2$  gas discharge were measured using a coherent anti-Stokes Raman spectroscopy system in the folded BOXCARS configuration. The discharge was in slowly flowing nitrogen between two parallel molybdenum electrodes. Current densities were  $0.047 \text{ A/cm}^2$  with an E/N of approximately 50 Td. The nearly wall-less discharge was stabilized using a Macor ceramic cap covering the cathode with a 9-mm circular aperture in the center. Measurements were made at spatially resolved locations within the discharge both axially and radially. Theoretical spectra were fit to experimental data to obtain the rotational and vibrational temperatures and the relative population.

A detailed study of the spectral line shape of the dye laser used as the probe beam in the CARS system was carried out using the optogalvanic effect in a Fe-Ne hollow-cathode lamp. Spectral line width and lineshape, under differing dye pumping schemes, were obtained. Measured line widths were greater than expected and showed a non-Gaussian profile for the probe laser. Nitrogen discharge stability was studied to determine conditions under which the discharge remains stable. Instability was noted visually and both the CARS signal and the electrode voltage showed hysteresis. For the future, a new CARS system was designed which will allow study of various gasses under differing discharge conditions.

Coherent Anti-Stokes Raman Spectroscopy, nitrogen discharge, nitrogen  
glow discharge, nitrogen rotational and vibrational temperature

96

Unclassified

Unclassified

Unclassified

Unlimited

## ABSTRACT

### CARS TEMPERATURE MEASUREMENTS AND STABILITY STUDIES OF A D.C. NITROGEN DISCHARGE

Michael Millard, M.S. Electro-Optics

University of Dayton, June 1991

Advisor: Dr. Perry Yaney

The vibrational and rotational temperatures of a 30-Torr, normal glow  $N_2$  gas discharge have been measured using a coherent anti-Stokes Raman spectroscopy system in the folded BOXCARS configuration. The discharge was set up in slowly flowing nitrogen between two plane parallel molybdenum electrodes. Current densities of  $0.047 \text{ A/cm}^2$  were used with an  $E/N$  of approximately 50 Td. The nearly wall-less discharge was stabilized using a Macor ceramic cap covering the cathode with a 9-mm circular aperture in the center. Measurements were made at spatially resolved locations within the discharge both axially and radially. Theoretical spectra were fit to experimental data in order to obtain the rotational and vibrational temperatures and the relative populations.

A detailed study of the spectral line shape of the dye laser used as the probe beam in the CARS system was carried out using the optogalvanic effect in a Fe-Ne

hollow-cathode lamp. The spectral line width and lineshape, under differing dye pumping schemes were obtained. These measured line widths were greater than had been expected and showed a non-Gaussian profile for the probe laser. Stability of the nitrogen discharge was also studied in order to determine the conditions under which the discharge remains stable. Instability was noted visually, in the behavior of the CARS signal and the electrode voltage, both of which showed hysteresis. In order to make way for changes in the system in the future, a new CARS system was designed which will allow study of various gasses under differing discharge conditions.

<b>Accession For</b>		
NTIS GRA&I	<input checked="" type="checkbox"/>	
DTIC TAB	<input type="checkbox"/>	
Unannounced	<input type="checkbox"/>	
Justification		
By		
Distribution/		
Availability Codes		
Dist	Avail and/or	Special
A-1		

## TABLE OF CONTENTS

ABSTRACT .....	iii
LIST OF TABLES .....	vii
LIST OF FIGURES .....	viii
ACKNOWLEDGMENTS .....	xi
CHAPTER	
I. INTRODUCTION .....	1
Research Focus	
CARS Overview	
Optogalvanic Overview	
II. THEORY .....	5
The CARS Process	
CARS Susceptibility	
Nitrogen Spectra	
Vibrational Excitation and De-Excitation	
Glow Discharge Theory	
The Cathode Region	
The Negative Glow	
The Positive Column	
The Anode Region	
The Optogalvanic Effect	
III. EXPERIMENT .....	24
Experimental CARS System	
Optogalvanic Setup	
IV. DATA AND ANALYSIS I .....	33
Motivation	
Dye Laser Evaluation	
Discharge Instability	
V. DATA AND ANALYSIS II .....	48

	Motivation	
	New Experimental Data	
	Analysis of Data	
VI.	CONCLUSIONS AND RECOMMENDATIONS .....	71
	Conclusions	
	Dye Laser Evaluation	
	Discharge Instability	
	New CARS Data	
	Recommendations	
REFERENCES	.....	75
APPENDICES		
A.	NEW CARS SYSTEM .....	83



## LIST OF TABLES

1.	CARS geometries, descriptions and comments .....	9
2.	Epling and Yaney's discharge conditions .....	34
3.	Cirillo and Yaney's discharge conditions .....	34
4.	Discharge conditions for data of Figures 29 and 30 .....	55
5.	Discharge conditions for data taken after Figures 29 and 30 .....	55
6.	Rate constants used to calculate V-T and V-V rates .....	67

## LIST OF FIGURES

1.	Processes contributing to the CARS signal .....	8
2.	Beam patterns of the three CARS geometries .....	8
3.	Degrees of freedom associated with a diatomic molecule .....	12
4.	Vibrational-rotational energy level diagram of diatomic molecule ...	13
5.	Transitions being studied .....	14
6.	Voltage-current characteristics of a parallel plate discharge .....	17
7.	Parallel plate discharge regions .....	18
8.	Basic hollow-cathode discharge configuration .....	21
9.	CARS optical system .....	25
10.	CARS data acquisition system .....	27
11.	Typical power curve of HyperDye 300 laser using Suforhodamine 640 .....	28
12.	Diagram of discharge chamber .....	29
13.	Optogalvanic optical system .....	30
14.	Optogalvanic data acquisition system .....	31
15.	Optogalvanic circuit .....	32
16.	Typical narrow-band CARS spectrum .....	35
17.	Expanded section of higher J lines in a typical narrow-band spectrum .....	36
18.	Lineshape of dye laser .....	37
19.	Probe files for use with Sandia CARS fitting code .....	38
20.	Refits of data from Figure 17 using new probe files .....	39

21.	Square root of CARS signal versus supply current .....	41
22.	Square root of hot band to ground state band ratio versus supply current .....	42
23.	Data showing hysteresis of electrode voltage .....	43
24.	Multimoding of positive column .....	45
25.	Spot formation as a function of electrode current .....	46
26.	Axial temperature profile from Cirillo .....	48
27.	Vibrational temperature measurements centered on region of the jump in Cirillo's data .....	50
28.	Rotational temperature profiles corresponding to Figure 27 .....	50
29.	Vibrational temperature profile obtained after centering the discharge at each axial position .....	53
30.	Rotational temperature profiles corresponding to Figure 29 .....	53
31.	CARS spectra, 8 mm from cathode .....	55
32.	Comparison of 12 mm and 14 mm vibrational temperature profiles .....	56
33.	Comparison of 12 mm and 14 mm vibrational temperature profiles .....	56
34.	2-Dimensional vibrational temperature profiles of discharge .....	57
35.	2-Dimensional rotational temperature profiles of discharge .....	57
36.	Spectra including the second hot band .....	58
37.	Comparison of radial vibrational temperature profiles taken at the same axial location within the discharge .....	60
38.	Comparison of radial rotational temperature profiles taken at the same axial location within the discharge .....	60
39.	2-Dimensional ground state band and first hot band profiles .....	62
40.	Integrated signal versus inverse rotational temperature .....	63
41.	Deviation of Treanor distribution from Boltzmann distribution .....	70
A1.	New CARS optical system .....	83

A2.	Pump beam splitter .....	84
A3.	3-Dimensional view of entrance to spectrometer in new CARS system .....	84
A4.	New discharge chamber .....	85

## ACKNOWLEDGEMENTS

As with any project such as this, there are a great many people without whose help this work would not have been possible. First and foremost, I would like to thank Dr. Perry Yaney for allowing me to work with him and learn from him more than I ever thought possible in a single year. I would also like to thank him for his advice on experiments, school work and life in general. It helped more than I can possible express.

I would also like to thank many of the people with whom I have had the extreme honor of working with and learning from while at Wright-Patterson AFB. These include, but are not limited to, Mr. Don Linder for all the wonderful equipment and stories he has supplied, Dr. Alan Garscadden and Dr. Charles DeJoseph for their continual guidance and humor, Dr. Bish Ganguly for his help in many areas and Mr. Mike Ray for his help and friendship.

Special thanks goes to Dr. Charles DeJoseph of Wright-Patterson AFB and Dr. Leno Pedrotti of the University of Dayton for their help in preparing and critical review of this work. I would also like to thank them for just being good friends. I hope that in the future I have the good fortune in working with such a tremendous group of people.

Finally, I would like to thank my many friends and my family for their support and kindness during these last two years, especially Carol and Gaylon Millard, my parents.

This project was funded by the Aero Propulsion and Power Laboratory at Wright-Patterson AFB under the Scholarly Research in Aerospace Power Program. The principal investigator of the program is Dr. Gary Thiele, Associate Dean and Director of Graduate Studies and Research in Engineering at the University of Dayton.

## CHAPTER I

### INTRODUCTION

In this chapter, a statement of the research focus is given. In addition, two short overviews of the two major research tools used in this work are presented here, namely coherent anti-Stokes Raman spectroscopy (CARS), used in the discharge diagnostics, and the optogalvanic effect (OGE), used in studying the dye laser in the CARS system.

#### Research Focus

Over the past several years this project, summarized in a final report by Yaney,<sup>1</sup> has been continued, expanded and refined by Emmerich,<sup>2</sup> Hodson,<sup>3</sup> Olesky,<sup>4</sup> Epling,<sup>5</sup> and Cirillo.<sup>6</sup> Their work entailed construction and subsequent modification and refinement of a CARS system to measure the vibrational and rotational temperatures in a N<sub>2</sub> discharge. The discharge was maintained in a parallel-plate electrode, D.C. glow configuration, with the gas flowing through the chamber. The work presented here is a continuation and a clarification of their work. The main objective of this work was to resolve some of the irregularities in the data collected by these researchers. Namely, to find the conditions in which the discharge is stable and reproducible and to characterize this discharge. A detailed study of the probe dye laser using the OGE was carried out to determine its effect on the high-resolution data taken by Yaney and Cirillo. Finally, the system has been modified in order facilitate a move of the experiment to a new location.

### CARS Overview

In 1928, C.V. Raman observed the scattering of photons from a molecule via inelastic collision.<sup>7</sup> Two things may happen when a photon and a molecule interact via an inelastic collision. First, a portion of the energy of the photon can be transferred to the molecule. In this case the scattered photon is down shifted in frequency because the molecule is undergoing a transition to a higher vibrational or rotational energy level. This Raman process is referred to as a Stokes shift. Secondly, if the molecule is already in an excited state, the photon can cause the de-excitation of the molecule, thus leaving it in a lower energy level. This means that the scattered photon will be up-shifted in frequency and is said to be anti-Stokes shifted.

Since the advent of the laser in the early 1960's, Raman scattering has become a very useful tool in spectroscopy. This arises from the unique character of the Raman spectrum observed for every particular medium or specimen probed by this technique. Raman scattering is a spontaneous process which is directly proportional to the incident irradiance. In spontaneous Raman scattering, not only is the light scattered over  $4\pi$  steradian, but the signal is also very weak and difficult to collect. Normally, photon counting is necessary, often a very time consuming technique. Nonlinear Raman processes such as coherent anti-Stokes Raman spectroscopy (CARS), however, can produce a laser-like output which can be many orders of magnitude greater than spontaneous scattering. Because the signal is a beam rather than spread over  $4\pi$  steradian, the beam does not suffer from the usual background problems of spontaneous Raman and can offer a high signal-to-noise ratio allowing fast detection techniques to be used. If pulsed lasers are used which operate in the visible region of the spectrum, the acquisition of the signal is greatly simplified because the CARS signal will also be in the visible. A photomultiplier tube, most sensitive in the visible, coupled to an analog-to-digital converter, is commonly used to generate the signal.

Although first demonstrated in 1963 by Terhune and Maker,<sup>8</sup> the CARS process was not developed into a diagnostic tool until 1973 by Regnier and Taran.<sup>9</sup> The usefulness of the CARS process comes from its ability to probe with very small control volumes and high spectral and temporal resolution (less than  $0.05\text{ cm}^{-1}$  and 8 ns, respectively). Since the early 1980's, the technique has been used in such hostile environs as jet engines, coal gasifiers, furnaces, liquid and solid propellants, lubricants under stress, gasses, flames and plasmas to measure species concentrations and temperatures where other techniques were not functional or disturbed the medium being probed.<sup>10</sup>

Although CARS has many advantages, it is not perfect. The technique requires high-peak power pulsed lasers and a tunable laser source for narrow-band probing, which can together easily cost well over \$100,000. The technique is also not suitable for probing minority species in most cases. This is because their relatively low partial pressure, and thus their low number densities, produces a weak CARS signal which is not easily measured. Finally, the medium being probed needs to be optically accessible. This means entrance and exit windows are needed to allow the laser beams to enter the medium and the CARS beam to leave. Often this is difficult to accomplish.

### Optogalvanic Effect Overview

The optogalvanic effect was first described by Penning in 1928. He noticed that when the light from a neon lamp fell onto a neon discharge which he was studying, there was a decrease in the impedance of the discharge, or, conversely, a rise in the conductivity. Although a known phenomena for many years thereafter, it was not until the advent of the tuneable dye laser that the optogalvanic effect (OGE) was studied more carefully. In the OGE, when a tunable light source, usually a dye laser, scans the wavelength corresponding an atomic transition of either the gas used in a discharge, or



of the material used as an electrode, there is a corresponding change in the conductivity of the discharge. Thus, detection of the optogalvanic signal is very straightforward, one only need monitor the current through the cell or measure the voltage across it.

The effect has only recently been modeled for a few simple cases. The difficulty lies in the fact that to model OGE, rate equations are needed. For only moderately complex cases, the number of equations becomes too large to solve in closed form. Also hampering efforts has been a lack of cross sections for the mechanisms involved.

Even so, the effect has been developed for a wide array of uses. Examples of which are, gas discharge diagnostics and for wavelength determination and laser calibration. The reason for its wide acceptance is its ease of use and the relatively simple experimental setup. The availability of commercial optogalvanic cells in the form of simple parallel plate discharges or hollow cathode lamps made of a wide variety of electrode materials and gasses giving a possible atomic transition in practically any lasing wavelength range.

## CHAPTER II

### THEORY

In this chapter, the CARS process will be summarized, including the non-linear optical phenomenon on which it is based. The observed signal will be related to the CARS susceptibility. Reviews of the characteristics of the spectrum of molecular nitrogen and glow discharge devices are given. A brief review of the optogalvanic effect is also included.

#### The CARS Process

The response of any medium to an incident radiation field of sufficiently high irradiance will be nonlinear. Nonlinear effects arise from interactions of coherent light with the electric polarization of the medium. This polarization arises from the polarizability of the individual units that make up the medium such as molecules. The polarizability is the proportionality constant which relates the polarization field to a weak incident field. The summation of the polarizability over a unit volume is called the susceptibility. In the presence of high electric fields, higher order terms, particularly the quadratic and cubic terms, must be included in the susceptibility. These higher order terms manifest themselves typically at high irradiances such as those in high power lasers. The interaction of the incident light with the medium induces oscillations in the polarization at various combinations of the driving frequencies of the incident sources. This in turn induces polarizations in the medium which then reradiate polarization waves at these combination frequencies. For isotropic molecular media, the polarization field

is given by

$$\vec{P} = \epsilon_0 \alpha \vec{E} \quad (1)$$

where  $\alpha$  is the polarizability of a molecule. The susceptibility is expanded in terms of the incident electric field can be written

$$\begin{aligned} \vec{P}_i(-\omega_i) = & \epsilon_0 \chi^{(1)}(-\omega_i) \cdot \vec{E}(\pm\omega_i) \\ & + \epsilon_0 \chi^{(2)}(-\omega_i; \omega_j, \omega_k) \cdot \vec{E}(\omega_j) \vec{E}(\omega_k) \\ & + \epsilon_0 \chi^{(3)}(-\omega_i; \omega_j, \omega_k, \omega_l) \cdot \vec{E}(\omega_j) \vec{E}(\omega_k) \vec{E}(\omega_l) \\ & + \text{higher order terms} \dots \end{aligned} \quad (2)$$

Here  $\vec{P}_i(-\omega_i)$  indicates the output polarization wave at frequency  $\omega_i$  and  $\vec{E}(\omega)$  indicates an incident electric field of frequency  $\omega_j$ .  $\chi^{(1)}$  is the linear susceptibility and  $\chi^{(2)}$  and  $\chi^{(3)}$  are the second and third order susceptibilities. The linear susceptibility is a tensor of rank two, a 3X3 matrix, while the second and third order susceptibilities are third and fourth rank tensors, respectively. Any process which takes two or more incident fields to create an output field is called a mixing process. Three-wave mixing is a  $\chi^{(2)}$  process in which two incident fields couple to generate a third at either the sum or the difference of the two input optical frequencies. Second harmonic generation is a degenerate case of three-wave mixing. In four-wave mixing, three intense optical fields interact with the third order susceptibility to produce a fourth field.

The CARS process is one of many nonlinear optical processes in which three intense electromagnetic fields generate a fourth beam inside a medium. This is nondegenerate four wave mixing. With CARS, three beams, two pump beams and a "Stokes" pump beam, of frequencies  $\omega_{p1} = \omega_{p2}$  and  $\omega_s$  respectively, couple through  $\chi^{(3)}$  to produce a fourth beam at  $\omega_{as} = \omega_{p1} + \omega_{p2} - \omega_s$ . The resultant frequency  $\omega_{as}$  of the output beam is up-shifted from the pump frequency and is called, therefore, the anti-

Stokes frequency.

When the frequency difference between the pumps and the Stokes beam matches a Raman resonance, the CARS signal at  $\omega_{as}$  is enhanced, i.e. the CARS signal intensity increases. There are, however, other processes which can contribute to the induced susceptibility,  $\chi_{\text{CARS}}$ . Figure 1 shows two common nonresonant, coherent scattering processes and the Raman process. When the molecular density is low, the signal due to these nonresonant processes are weak and vary slowly with wavelength in comparison to the resonant process, and therefore have negligible influence on the observed spectra.

In order for the energy and the momentum of the process to be conserved, as is required in a scattering process, the wave vector relationship between the four fields must be matched. That is,

$$\vec{k}_{as} = \vec{k}_{p1} + \vec{k}_{p2} - \vec{k}_s \quad (3)$$

where  $|\vec{k}| = \omega n/c$ . This wave vector, or phase, matching ensures that the signal generated inside the crossing of the three beams, called the interaction or control volume, will be in phase throughout the control volume. Any phase mismatch can lead to destructive interference between signal generated at different points within the control volume, thus reducing the total signal strength.

Several schemes have been devised in order to meet the phase matching requirements of CARS. Table 1 gives the most common configurations, a brief description of each process and a list of a few of their advantages and disadvantages. Figure 2 illustrates the beam patterns on the collecting lens of the CARS system. In the case of colinear CARS, the CARS beam is overwhelmed by the pump and both probe beams, while in planar BOXCARS, the signal is separated from the probe and one of the pump beams, but is still dominated by the other pump beam. In folded-BOXCARS, all four

beams are clearly resolved.

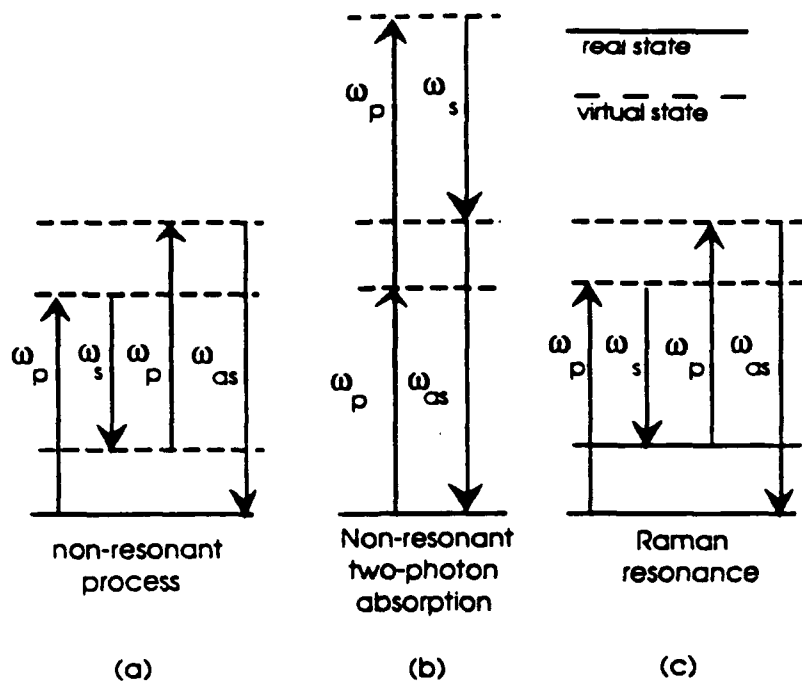


Figure 1. Processes contributing to the observed CARS Signal.  
 (a) and (b) produce nonresonant background signals.  
 (c) Resonant Raman process (resonance with a real state).

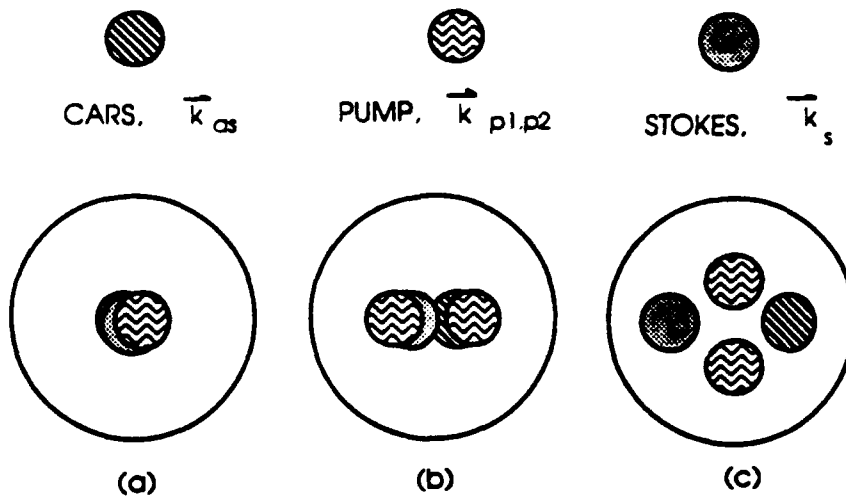
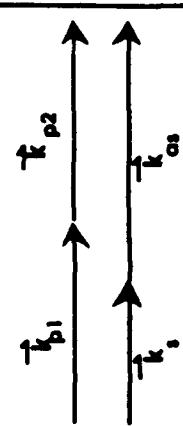
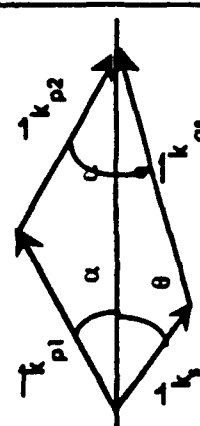
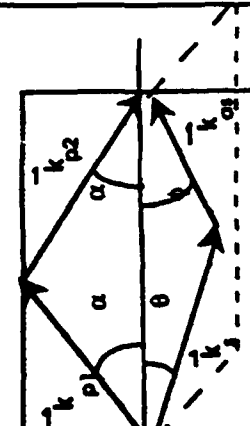


Figure 2. Beam patterns of the three different CARS geometries.  
 (a) Collinear CARS.  
 (b) BOXCARS.  
 (c) 3D or Folded BOXCARS  
 The beam separation is evident in (c), while in (a) and (b) the CARS beam is obscured by one or more of the laser beams.

Table 1. CARS geometries, descriptions and comments.

Process and vector diagram	Description	Advantages/Disadvantages
<p>(a) COLINEAR CARS</p> 	<p>The Wave vectors of the pumps and Stokes beams are collinear and overlap. This leads to the relation <math>k_p \approx k_{p2}</math> (4)</p> $k_{as} \approx 2k_p - k_s$ (5) <p>(Note: This is only true in the case <math>n_p \approx n_s</math>.)</p>	<p><b>Advantages:</b></p> <ol style="list-style-type: none"> <li>1) High CARS intensity.</li> <li>2) Large interaction/control volume.</li> </ol> <p><b>Disadvantages:</b></p> <ol style="list-style-type: none"> <li>1) CARS beam not separate from input beams.</li> <li>2) Poor spatial resolution.</li> </ol>
<p>(b) PLANAR BOXCARS</p> 	<p>Pump beams incident on the Stokes beam at angle <math>\alpha + \theta</math>. All three are coplanar. The pump beams are generated by splitting the beam from a single laser, then recombined at the proper angles and location. Phase matching is achieved when the following relations hold</p> $n_s \omega_s \sin \theta = n_{as} \omega_{as} \sin \phi$ (6) $n_s \omega_s \cos \theta + n_{as} \omega_{as} \cos \phi = 2n_p \omega_p \cos \alpha$ (7)	<p><b>Advantages:</b></p> <ol style="list-style-type: none"> <li>1) Greater spatial resolution.</li> <li>2) High CARS intensity.</li> </ol> <p><b>Disadvantages:</b></p> <ol style="list-style-type: none"> <li>1) CARS not separated from one pump beam.</li> <li>2) CARS intensity not as high as with colinear CARS</li> <li>3) Alignment difficult because of angular dependencies.</li> </ol>
<p>(c) 3D-FOLDED BOXCARS</p> 	<p>The two pump beams and the Stokes and anti-Stokes beams lie in different planes. When the two planes are at 90 degrees, the beams are maximally separated, giving the highest spatial resolution. Phase matching is again achieved when (6) and (7) hold.</p>	<p><b>Advantages:</b></p> <ol style="list-style-type: none"> <li>1) High spatial resolution.</li> <li>2) Small control volume.</li> <li>3) CARS beam separate from other beams.</li> </ol> <p><b>Disadvantages:</b></p> <ol style="list-style-type: none"> <li>1) Small CARS intensity compared to (b).</li> <li>2) Alignment sensitive to angles, motion, etc.</li> </ol>

### CARS Susceptibility

The total CARS susceptibility consists of a resonant and nonresonant term which we write as

$$\chi_{\text{CARS}}^{(3)} = \chi_R^{(3)} + \chi_{\text{NR}}^{(3)} \quad (8)$$

Nibler and Knighten<sup>12</sup> derived an expression for the resonant term in  $\chi_{\text{CARS}}^{(3)}$  given by

$$\chi_R^{(3)} = \frac{n_p c^4 \pi}{h n_s \omega_s^4} \left[ \frac{\partial \sigma}{\partial \Omega} \right] \sum_{m,r} \frac{N_m - N_r}{\omega_{r,m} - \omega_p + \omega_s - i \Gamma_{r,m}} \quad (9)$$

where,

$n_p, n_s$  = indices of refraction of pump and Stokes beams, respectively.

$h, c$  = Planck's constant and the speed of light respectively.

$N_r, N_m$  = Number densities of the  $r^{\text{th}}$  and  $m^{\text{th}}$  energy level, respectively.

$\left[ \frac{\partial \sigma}{\partial \Omega} \right]$  = Differential Raman cross section.

$\omega_p, \omega_s$  = The frequencies of the pump and Stokes beams, respectively.

$\omega_{r,m}$  = The Raman resonance frequency

$\Gamma_{r,m}$  = Raman line widths (HWHM).

An important feature of this expression is that the susceptibility is proportional to the *difference* in populations of the two energy states. The weak nonresonant term is generally neglected since it was constant over the measured spectra.

The resulting CARS irradiance for colinear CARS given by Eckbreth<sup>13</sup> is

$$I_{\text{as}} = \frac{\omega_{\text{as}}^2}{n_p^2 n_s n_{\text{as}} c^4 \epsilon_0^2} I_s I_p^2 |\chi_{\text{CARS}}^{(3)}|^2 l^2 \text{sinc}^2\left(\frac{\Delta k l}{2}\right) \quad (10)$$

where,

$I_s, I_p$  = The Stokes and pump beam intensities respectively.

$l$  = Interaction length.

$\epsilon_0$	=	Permativity of free space.
$\Delta k$	=	Phase mismatch ( $\Delta k=0$ for phase matching).
$\omega_{as}$	=	Frequency of anti-Stokes beam (CARS beam).
$n_{as}$	=	Index of refraction of anti-Stokes beam.

From this expression for the observed irradiance, it can be seen that the CARS beam intensity is sensitive to intensities of the input beams, interaction length and alignment (phase matching term,  $\Delta k$ ). In the system used here, the dye laser used as the probe (Stokes) beam is pumped by the same laser used for the pump beams, i.e.  $I_s \propto I_p$ . Thus, the CARS beam is proportional to the *cube* of the pump beam,  $I_{as} \propto I_p^3$ . Because of this dependency, any fluctuation in the pump beam can have a drastic effect on the CARS intensity. The CARS signal is also sensitive to pressure. This is because the intensity is proportional to the square of the susceptibility, the susceptibility is proportional to the difference of the energy state populations, and thus the CARS signal is sensitive to populations or equivalently, when in thermal equilibrium, the pressure.

### Nitrogen Spectra

In order to understand the spectra obtained from a CARS system, it is important to understand how the molecular energy levels are both spaced and populated. For a diatomic molecule, the energy levels are characterized by their rotational-vibrational population distribution. Homonuclear diatomic molecules such as nitrogen can be best described as a nonrigid rotator. This is different from the rigid rotator and anharmonic oscillator model sometimes used.<sup>14</sup> A full development of the nonrigid rotator is beyond the scope of this work, therefore only the relevant points are summarized here.

A molecule has several degrees of freedom. A diatomic molecule has six; three translational, two rotational and one vibrational, as illustrated in Figure 3. These



degrees of freedom lead, in turn, to translational, rotational and vibrational energy states of the molecule.

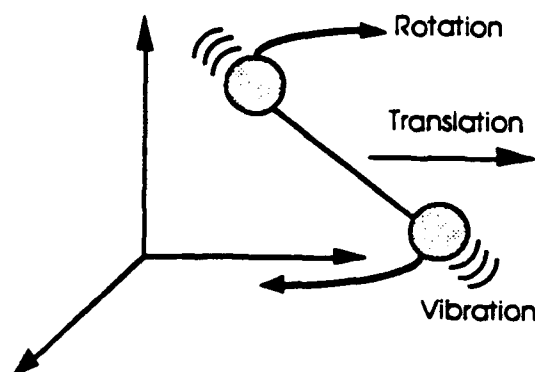


Figure 3. Degrees of freedom associated with a diatomic molecule. The atoms vibrate as the molecule rotates.

The vibrational and rotational energy states are given by<sup>14</sup>

$$G(v) = \omega_e \left( v + \frac{1}{2} \right) - \omega_e x_e \left( v + \frac{1}{2} \right)^2 + \dots \quad (11)$$

and,

$$F_v(J) = B_v J(J+1) - D_v J^2(J+1)^2 + \dots \quad (12)$$

where,

$$B_v = B_e - \alpha_e(v+1/2) + \dots$$

$$D_v = D_e - \beta_e(v+1/2) + \dots$$

$\omega_e, B_e, D_e, \alpha_e, \beta_e, x_e$  are all constants in  $\text{cm}^{-1}$ .<sup>15</sup>

$J$  = Rotational quantum number = 0, 1, 2, ...

$v$  = Vibrational quantum number = 0, 1, 2, ...

The total energy of the system (in  $\text{cm}^{-1}$ ) is thus

$$E_{v,J} = G(v) + F_v(J) \quad (13)$$

An energy level diagram corresponding to these energy states is given in Figure 4.

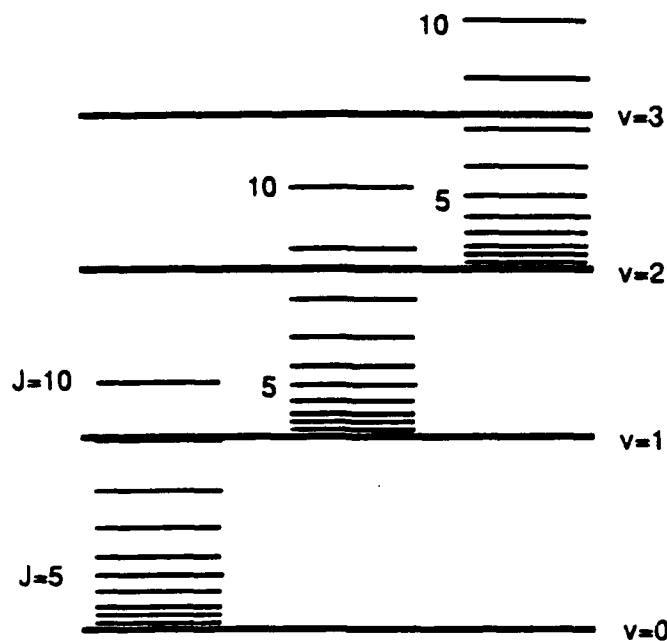


Figure 4. Approximate vibrational-rotational energy level diagram of a diatomic molecule.<sup>14</sup>

The selection rules for Raman transitions of diatomic molecules are  $\Delta v = 0 \pm 1$  and  $\Delta J = \pm 1, \pm 2$ . These allow for several possible sets of transitions. Since homonuclear diatomic molecules do not possess a permanent dipole moment, infrared transitions are forbidden. Vibrational Raman scattering does occur for  $\Delta J = 0$ . In the case of  $\Delta J = 0$  and  $\Delta v = \pm 1$  we have the so called Q-branch of nitrogen. The process occurs when the difference in frequency between photons from the two pump beams and the probe beam falls within the linewidth of a Raman transition in the molecule, as illustrated in Figure 5.<sup>16</sup> That is, the anti-Stokes frequency exactly matches a frequency within a transition from a molecule in the  $v, J$  state to the  $v+1, J$  state. It must be noted that this process does not occur in a sequence of events, rather the entire process is instantaneous, with the exchange of photons occurring simultaneously and the virtual states exist only during the process and collapse when it is completed.

In the work reported here, measurements were made of the  $v=0$  to  $v=1$  transitions called the ground state band,  $v=1$  to  $v=2$  transitions, the first hot band, and  $v=2$  to  $v=3$ , the

second hot band. Figure 5 is an energy level diagram showing a ground state band transition in the CARS process.

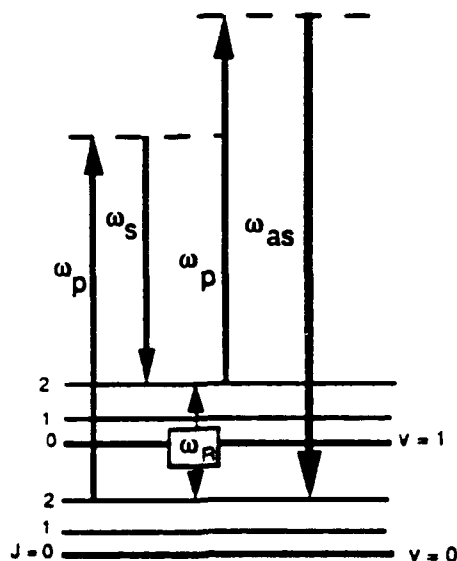


Figure 5. The actual transitions being studied. Dashed lines indicate virtual states, solid lines refer to real states.  $\omega_R$  is the Raman resonance frequency.

At a temperature  $T$ , the equilibrium populations of these energy levels are determined by the Maxwell-Boltzmann distribution<sup>14</sup> given by

$$N_{v,J} = \left( \frac{g_J N (2J+1)}{Z} \right) \exp \left[ - \frac{E_{v,J} hc}{k_B T} \right] \quad (14)$$

where,

- $g_J$  = Nuclear degeneracy.
- $N$  = The total number density.
- $Z$  = The partition function which normalizes the distribution to give the fraction of the total number density in a given energy state.
- $J$  = The rotational quantum number.
- $k_B$  = Boltzmann's constant.

Inside a dc discharge, however, the system is not in rotational-vibrational equilibrium.

Because of the non-equilibrium conditions, the populations can be expressed in terms

of separate Boltzmann vibrational and rotational factors, which are called temperatures although they do not represent any real temperature of the system since a temperature denotes an equilibrium condition.<sup>17-20</sup> Eq.(14) may then be rewritten as

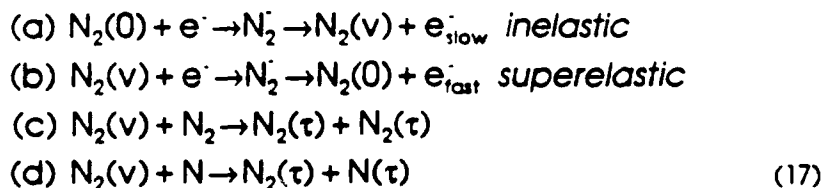
$$N_{v,J} = \left( \frac{g_J N(2J+1)}{Z_n} \right) \exp \left[ \frac{G(v)hc}{k_B T_v} \right] \exp \left[ \frac{F_v(J)hc}{k_B T_R} \right] \quad (15)$$

where,  $T_v$  and  $T_R$  are the vibrational and rotational temperatures. The partition function,  $Z_n$ , is given by

$$Z_n = \sum_v \sum_J g_J (2J+1) \exp \left[ \frac{-G_v hc}{k_B T_v} \right] \exp \left[ \frac{-F_v(J) hc}{k_B T_R} \right] \quad (16)$$

### Vibrational Excitation and De-Excitation

Because the discharge studied here is nearly wall-less, and dipole radiation by the  $N_2$  molecule is forbidden, the vibrational excitation and de-excitation of the gas is limited to only a few processes. These are, recombination of two N atoms to form a molecule, the recombination of an electron and  $N_2^+$  into vibrationally excited nitrogen, vibrational energy exchange among  $N_2$  molecules, and the following:



In process 17(a) above, neutral nitrogen captures a low energy electron forming the unstable, short-lived  $N_2^-$  ion. The low energy electron loses some of its energy when  $N_2^-$  quickly decays to vibrationally-excited neutral  $N_2$  plus a lower energy electron. In the reciprocal process 17(b), a low-energy electron is captured by vibrationally-excited nitrogen, which gives up some of its energy forming neutral nitrogen and a higher energy electron. In processes 17(c) and 17(d), vibrationally excited nitrogen collides with either  $N_2$  or N converting the vibrational energy to translational energy ( $\tau$ ). In the

absence of radiative decay, the vibrational state population of the gas must be a balance of these processes.

Since the rotational-translational collision cross section is much greater than that of vibrational-translational collisions, the rotational states populated within each vibrational state reach an equilibrium with the translational temperature. Thus, the rotational temperature is taken to be the thermodynamic temperature of the gas. The vibrational states, however, do not reach this equilibrium state and show a much higher vibrational temperature than the rotational temperature. Since one may obtain the rotational temperature of the gas directly from CARS spectra, one of the main goals of this research was to characterize the discharge temperatures, both rotational and the vibrational.

The electron energy in the positive column (described below) has its maximum in the 1.8 to 3.0 eV range. This also happens to be the energy range for which the cross section of the formation of  $N_2^+$  is at its maximum.<sup>21</sup> Because the mass of the electron is negligible compared to the mass of the positive ions, the electrons have a higher velocity than the ions raising the collision rate between electrons and ions to well above the collision rate for molecule-molecule collisions. This means, in effect, that the rate of production of vibrationally excited nitrogen is not only a function of molecule-molecule collisions, but is also a function of electron-molecule collisions.

### Glow Discharge Theory

The main objective of the work presented here is a basic characterization of a nitrogen glow discharge by means of CARS. In order to evaluate the results to be presented, it is helpful to describe the basic properties and regions of a typical glow discharge and to introduce some of the terms used to describe them. This section will be a brief, qualitative description of a normal glow discharge.

The discharge under study consists of two plane parallel electrodes in a nitrogen gas medium across which a voltage is applied. Normally, gasses are good insulators, but as the voltage applied to the electrodes is increased, a discharge will strike and current is set up in the gas. Figure 6 gives the voltage-current characteristics of a low pressure, direct-current discharge including the names of the different discharge regions. As can be seen from the diagram, in the normal glow region, the current may be varied slightly (a factor of around 10, from  $10^{-3}$  Amp. to around  $10^{-2}$  Amp.) without an appreciable change in the voltage across the electrodes and is therefore relatively stable. The discharge studied in the work reported here, operated in the normal glow region.

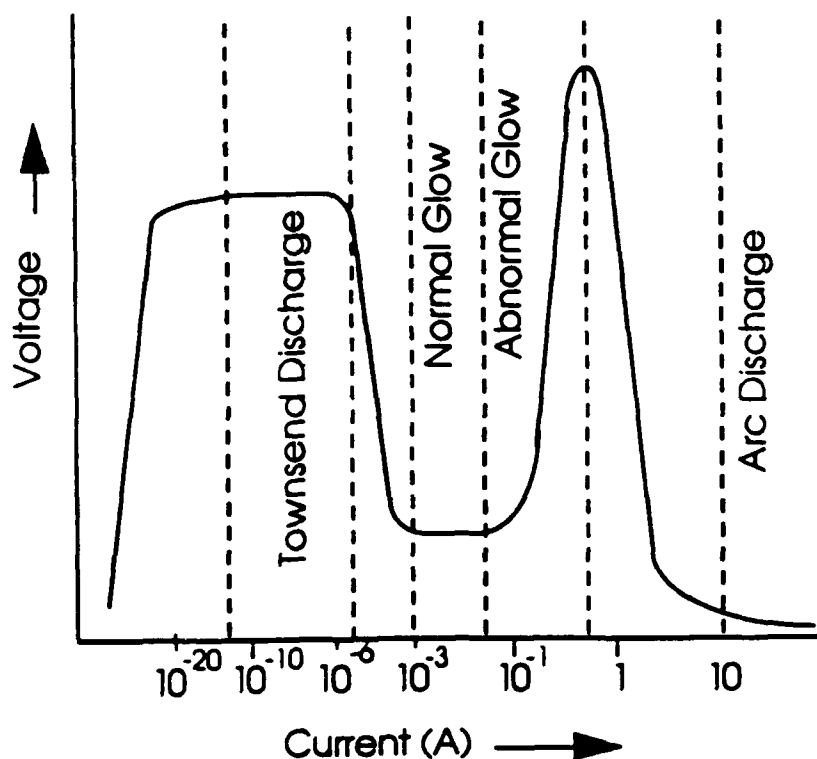


Figure 6. Voltage-current characteristics of a parallel plate discharge.<sup>27</sup>

Within such a discharge, there appear separated zones which may be distinguished visually. Figure 7 shows these different regions within a confined discharge as well as electric field, potential, current and space-charge density characteristics of

the discharge as a function of axial position. What follows is a brief description of these zones.

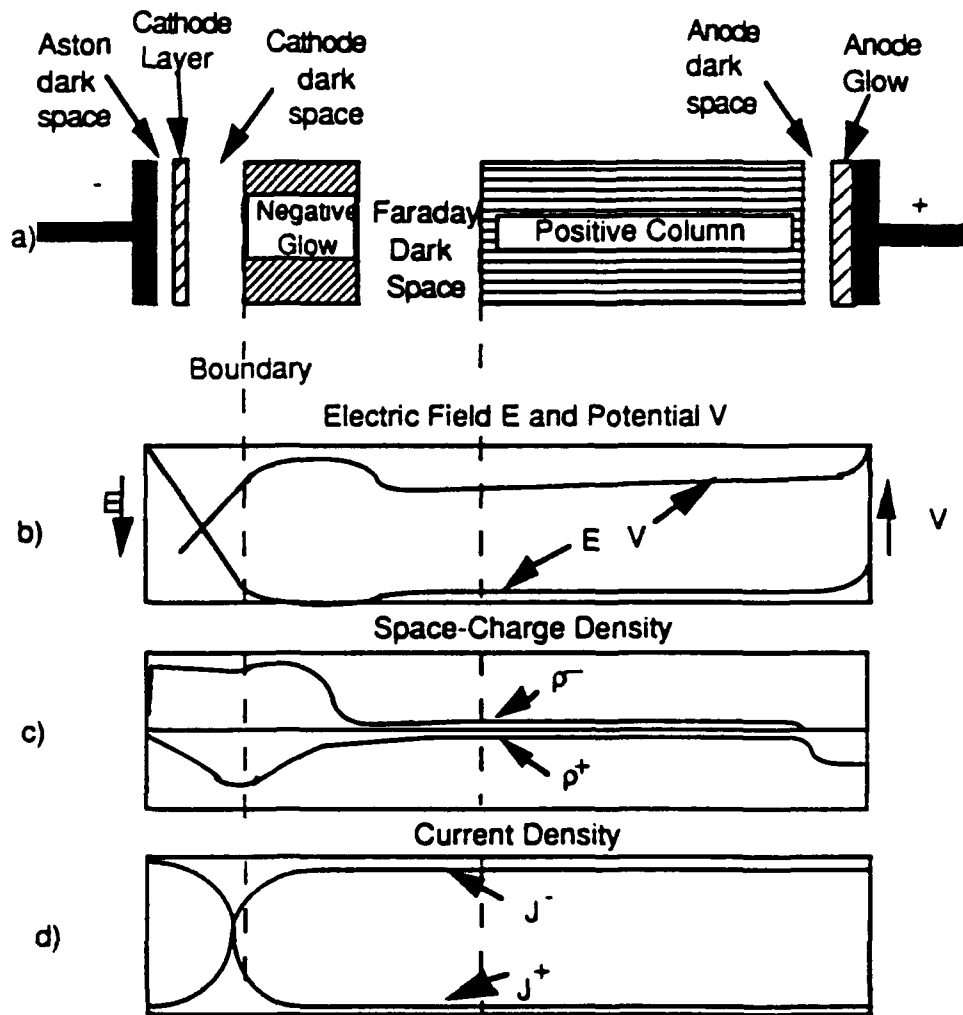


Figure 7. a) Visible features of a parallel electrode glow discharge.  
 b) Axial electric field and potential variations.  
 c) Axial space charge density variation.  
 d) Axial current density variation.

### The Cathode Region

In the cathode region, low-energy electrons (near 1 eV) are created at the cathode as positive ions strike the surface. Immediately after the cathode surface, the electrons have not yet reached the velocity (energy) needed to ionize the gas. Thus,

there is a buildup of electrons and the space charge density is negative. Also, because the electrons do not have the energy to ionize, the luminosity of this zone is very low. This region is called the Aston Dark Space. As the electrons are accelerated away from the cathode, they pickup energy and begin to ionize the gas. As they ionize and recombine with incoming positive ions, the discharge begins to glow faintly. This is known as the cathode glow region. As the pressure is lowered, fewer and fewer positive ions are available for recombination with the electrons. The result is a nearly perfect electron beam in this area.

Directly following the cathode glow, comes the cathode dark space. Here, an abundance of electrons slowed by inelastic collisions but with energy too great for electronic excitation, ionize the gas very efficiently. This ionization creates an electron cascade of fast moving electrons. Due to the different mobilities of electrons and positive ions, there is an over all build up of positive ions causing a net positive space charge density. Since there is little or no ionization or recombination in this area, the luminosity is low and a dark space is created. This cathode region is, in general, known as the cathode fall region because of the drop in potential between the two dark spaces.

### **The Negative Glow**

The negative glow is marked by a sharp rise in luminosity. At this point the electrons produced in the cathode region have lost much of their energy through ionization and collisions. These low-energy electrons are perfect for excitation of the gas through inelastic collisions. The low electric field in this region means that there will be a sharp rise in recombination of electrons and positive ions leading to a sharp rise in luminosity. As the distance from the cathode increases, the average electron energy begins to drop, the space charge density goes to zero and the electric field takes on a



small and fairly constant value, consequently, the luminosity drops off. This is the Faraday dark space.

### **The Positive Column**

Immediately following the Faraday dark space is the positive column. The small and relatively constant electric field value found in the Faraday dark space, extends itself throughout the positive column. In this region, the discharge constitutes a classic plasma. Since the electric field is small and constant, the positive column is basically neutral. This does not, however, imply that there are no charged elements in this area, rather the *net* charge is zero. The motion of the electrons in the positive column is no longer beam like, instead the motion is random, i.e. their random velocity becomes greater than their axial drift velocity. The luminosity of the positive column is relatively high because of ionization of the gas.

### **The Anode Region**

Very near the anode, the forces of electron attraction and ion repulsion create an increased electric field and a negative space charge density. Electrons from the positive column are accelerated by this increased electric field, raising the energy of the electrons above that for ionization or excitation. This creates the anode dark space. At the face of the anode, electrons strike the face of the electrode releasing positive ions and raising the luminosity of the region. This region is known as the anode glow.

### **The Optogalvanic Effect**

The mechanism by which one obtains a spectrum via the optogalvanic effect is much too complicated to be resolved for any but the simplest cases. Therefore, only a brief, qualitative discussion of the effect will be given here. The rate equations for a

simple hollow cathode discharge have been work out, and the results will be presented.<sup>21</sup>

When a tunable laser source is tuned near the wavelength of an atomic transition of one of the species present in a discharge, the electrical properties of the discharge are altered. The basic mechanisms which cause these changes are a variation in electron-ion pair production and a change of the electron and gas temperatures by super-elastic collisions.<sup>21</sup> In the case of a hollow-cathode discharge, the negative glow region is greatly enlarged, and the second of these two processes dominates which permits a solution to the rate equations governing the effect to be solved in closed form.

Inside the hollow cathode discharge, shown in Figure 9, there is a large electric field which accelerates ions against the cathode surface. Collision with the cathode

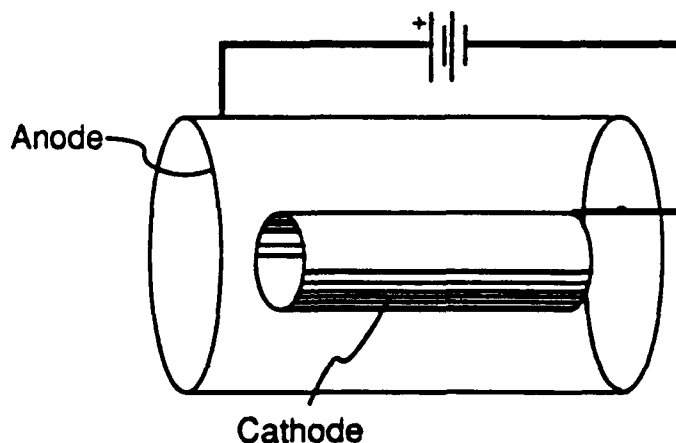


Figure 8. Basic hollow-cathode discharge configuration.

surface releases a large number of excited atoms and ions which can be used as a source of refractory elements. These atoms produced at the cathode surface are then excited by the incident laser radiation. Keller *et al.*<sup>22</sup> and Keller and Kalewski<sup>23</sup> found that the signal produced was independent of the ionization energy of the absorbing atoms and of the difference between the laser and the excited level the

medium.<sup>21, 24</sup>

With this knowledge, the signal can be explained by assuming that the system transfers energy from the laser radiation to electrons directly without seriously effecting the populations of the excited atoms. Because of frequent elastic and superelastic collisions between atoms and electrons, the electron temperature and the electronic excitation temperature of the atoms in the discharge are approximately equal. Laser radiation perturbs this process, but because the collisions are so frequent, any change in population is prevented. Therefore, the energy absorbed by the atoms from photons near a transition frequency is transferred to the electrons. This extra electron energy is manifested as a change in the impedance and of electron density in the discharge<sup>25</sup>. The corresponding change in conductivity in a neon discharge was found to be<sup>24</sup>

$$\frac{\Delta\sigma}{\sigma} = 1.5 \frac{\nu_{ei}}{\nu_{ei} + \nu_{ea}} \frac{\Delta T_e}{T_e} - \frac{\nu_{ea}}{\nu_{ei} + \nu_{ea}} \frac{\Delta N_e}{N_e} \quad (18)$$

where,

- $\sigma$  = Conductivity ( $\Delta\sigma$  = change in conductivity).
- $T_e$  = Electron temperature ( $\Delta T$  = change in electron temperature).
- $N_e$  = Electron density ( $\Delta N_e$  = change in electron density).
- $\nu_{ei}$  = Electron-ion collision frequency.
- $\nu_{ea}$  = Electron-atom collision frequency.

Because neon is a relatively light element, however, its Doppler width is a concern in comparison to the line width of the exciting dye laser. The Doppler width of a transition is given by<sup>16</sup>

$$\Delta\nu_D = \left( \frac{8RT \ln(2)}{Mc^2} \right)^{\frac{1}{2}} \nu_0 \quad (19)$$

where,

- $R$  = Gas constant (8.314 J/K/mol).  
 $T$  = Temperature (K).  
 $M$  = Atomic mass of medium (20 for neon).  
 $c$  = speed of light.  
 $\nu_0$  = Frequency of transition of interest.

The line shape of such a Doppler broadened transition is given by<sup>26</sup>

$$g(\nu) = \frac{2\sqrt{\ln(2)}}{\sqrt{\pi} \Delta\nu_D} \exp\left[-\frac{4(\ln(2))(\nu - \nu_0)^2}{\Delta\nu_D^2}\right] \quad (20)$$

Although slightly modified, this is the general equation for a Gaussian lineshape. Other mechanisms may also contribute to the observed line shape. The most prominent in the case of a gas discharge are power broadening and saturation. With power broadening, sometimes called saturation broadening, the intensity of the signal is inversely proportional to the intensity of the incident laser radiation and begins to limit the intensity of the observed signal while amplifying the wings of the line, i.e. the lineshape away from the center of the transition is amplified with respect to the central part of the transition. Once saturation occurs, the central part of the transition no longer responds to increases of incident laser irradiation and the signal becomes flat topped.

## CHAPTER III

### EXPERIMENT

In this chapter, the CARS optical system is described and a few of the important components and parameters of the system are discussed. The CARS data acquisition system is also described, including an explanation of how the optical signal is converted and transferred to computer disk for analysis. The optogalvanic setup is discussed along with the electronics needed to convert the signal to a useful form for analysis.

#### Experimental CARS System

The CARS system, illustrated in Figure 9, is essentially identical to that used by Cirillo and Yaney.<sup>9</sup> A 20 Hz Spectra Physics DCR-3 Nd:YAG laser, seeded by a Nd:YAG CW single mode injection laser, is operated in the Q-switch mode, doubled from its 1064 nm operating wavelength to 532 nm. The laser was typically operated at an output energy of nearly 210 mJ/pulse and, when seeded, a bandwidth of  $0.006 \text{ cm}^{-1}$ . Often, in order to shorten the time required to obtain a single spectrum, the laser was operated in the unseeded mode. The 532 nm output is split by a 35/65 beam splitter (BS1), the 35% beam being used to pump a Lumonics HyperDye-300 scanning dye laser, and the remaining 65% is used for the pump beams in the CARS process.

Since the Nd:YAG is used to pump the dye laser and the pulses of the pump and dye (Stokes) beams must reach the interaction volume at the same time, the path lengths of the two pump beams must be extended in order to allow the Stokes beam to

be generated inside the dye laser itself. Thus, the pump beams are split by a beam splitter (BS2) and the path lengths, and thus the pulse timing, are equalized by use of optical delay lines.

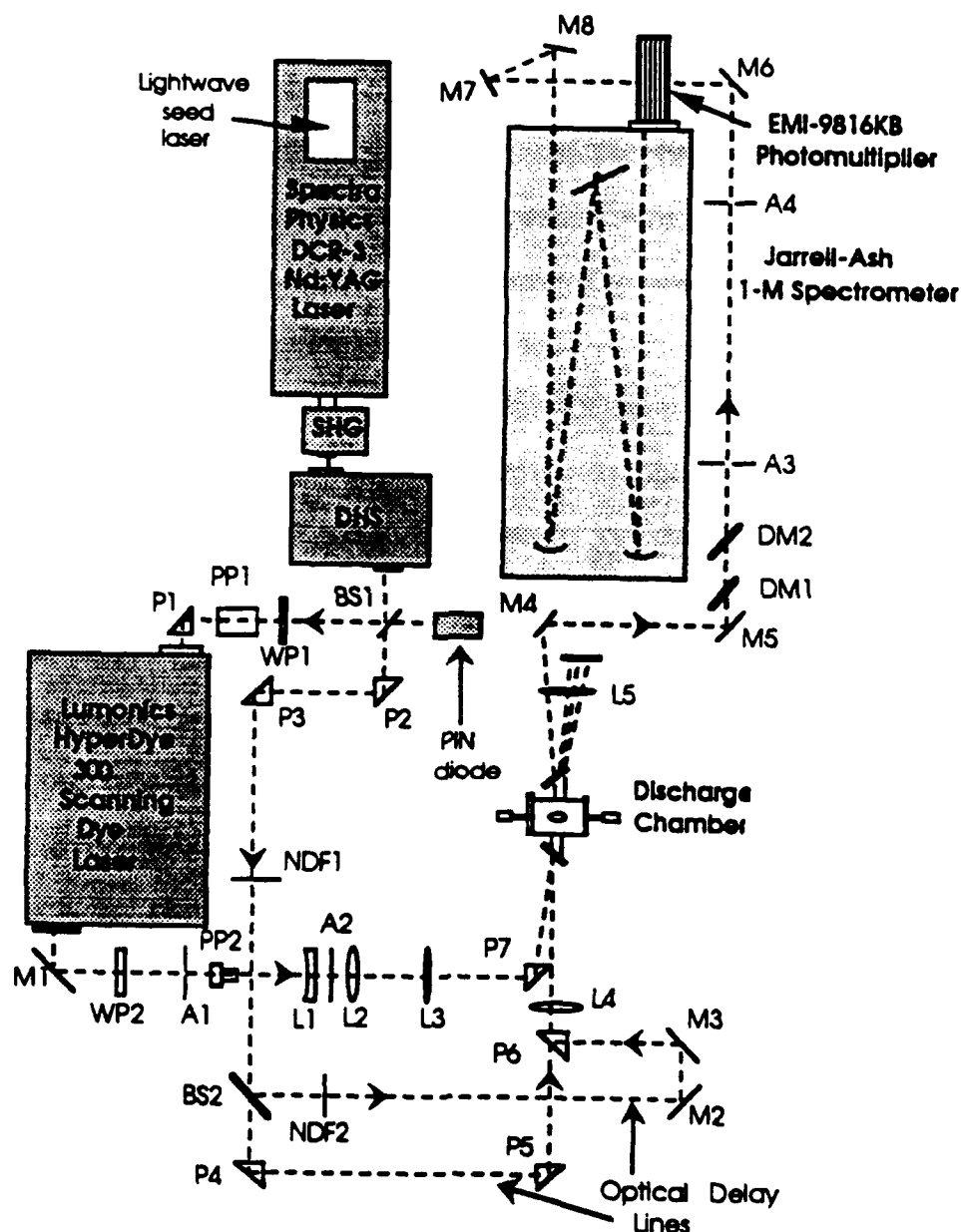


Figure 9. CARS optical system .

The only modification of the system from that used by Cirillo and Yaney<sup>6</sup> was the addition of a high power laser prism polarizer (PP1). Rotation of the half-wave plate

(WP1) provided easy control of the pumping power to the dye. The two pump beams and the Stokes beams are focused by two 500 mm lenses (L3, L4) into the discharge chamber. In order to ensure that the two pump beams are of equal power when they reach the interaction volume, a neutral density filter (NDF2) was placed in the path of the reflected beam to counter losses in the beam splitter.

After exiting the discharge chamber, the CARS beam was separated from the Stokes beam and the two pump beams by beam dumps designed to collect the three laser beams. Further filtering of the CARS beam to remove any trace of the three generating beams was accomplished by two dichroic mirrors (DM1, DM2) placed just after the steering mirrors (M4, M5). M4 through M8 are mirrors used to direct the CARS beam onto the spectrometer slit. The 1-m Jarrell-Ash Spectrometer was set at 474.7 nm and the spectral scanning of the sample was accomplished by tuning the dye laser. Detection of the CARS beam is accomplished by means of an EMI-9816KB photomultiplier tube (PMT) mounted to the spectrometer.

A block diagram of the data acquisition system is given in Figure 10. The signal from the PMT was delayed by a coaxial cable long enough to ensure that the signal pulse could be made to coincide with the gating pulse from the EG&G LG 105/N Linear Gate and Stretcher used in integrating the CARS pulse. The gating pulse was generated by a Hewlett-Packard 8012 pulse generator and a discriminator triggered by a PIN diode monitoring the pulses of the Nd:YAG laser. The integrated pulse from the linear gate and stretcher was then sent to the Nicolet 1170 signal averager where the CARS signal was digitized and stored. The Nicolet averaged over a set number of pulses of the Nd:YAG Q-switch for each point recorded. After recording a point, the Nicolet, via the Keithley unit, signaled the HyperDye scan control unit to move the grating to the next position. Normally for a high resolution scan, when the Nd:YAG laser was seeded, the line width was approximately  $0.006 \text{ cm}^{-1}$  and the signal was averaged over 90 shots with a step size

of 0.0015 nm. For a low resolution scan, when the Nd:YAG laser was unseeded, the line width was about 1.0 cm<sup>-1</sup> and the signal was averaged over 60 shots per point with a step size of 0.01. Scan time for a high resolution spectrum was nominally 90 minutes and 20 minutes for a low resolution scan.

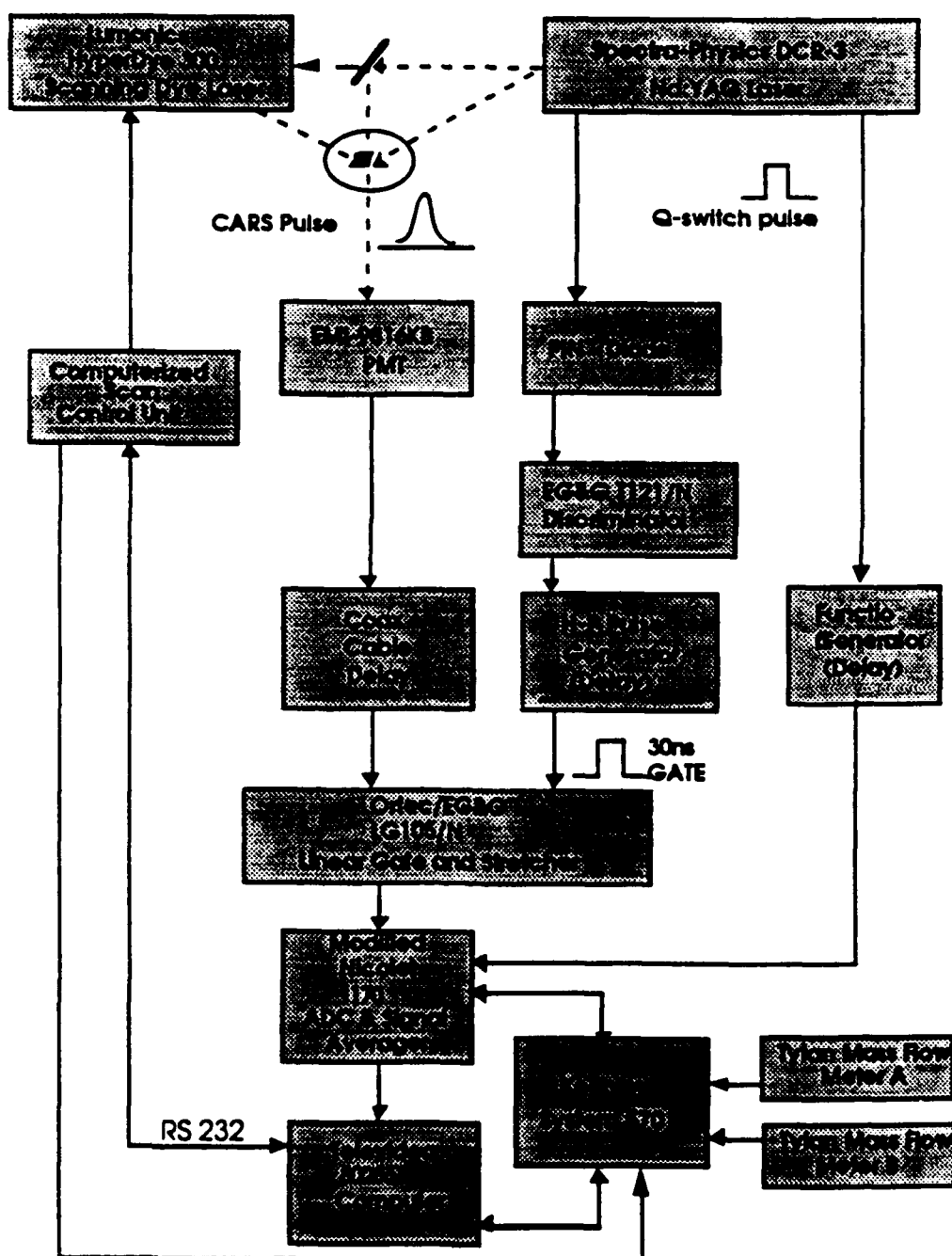


Figure 10. CARS data acquisition.



The flow of nitrogen through the chamber is monitored and statistics recorded from a Tylan electronic mass flow meter. The signal from the Tylan flow meter is obtained through a Keithley 570 data acquisition module connected to a 80286 based Televideo AT clone. The Keithley unit also allows for direct computer control of the signal averager and the dye laser scan control unit. After a whole spectrum was recorded, the scan control unit signaled the signal averager to stop recording data, and signaled the computer to start the down load procedure. The data was down loaded from the signal average to the Televideo computer for future processing and analysis. Sulforhodamine 640 in methanol was used in the dye laser for this experiment in order to obtain a scan range of approximately 602 nm to 608.8 nm. Figure 11 shows the intensity characteristics of this dye versus laser wavelength.

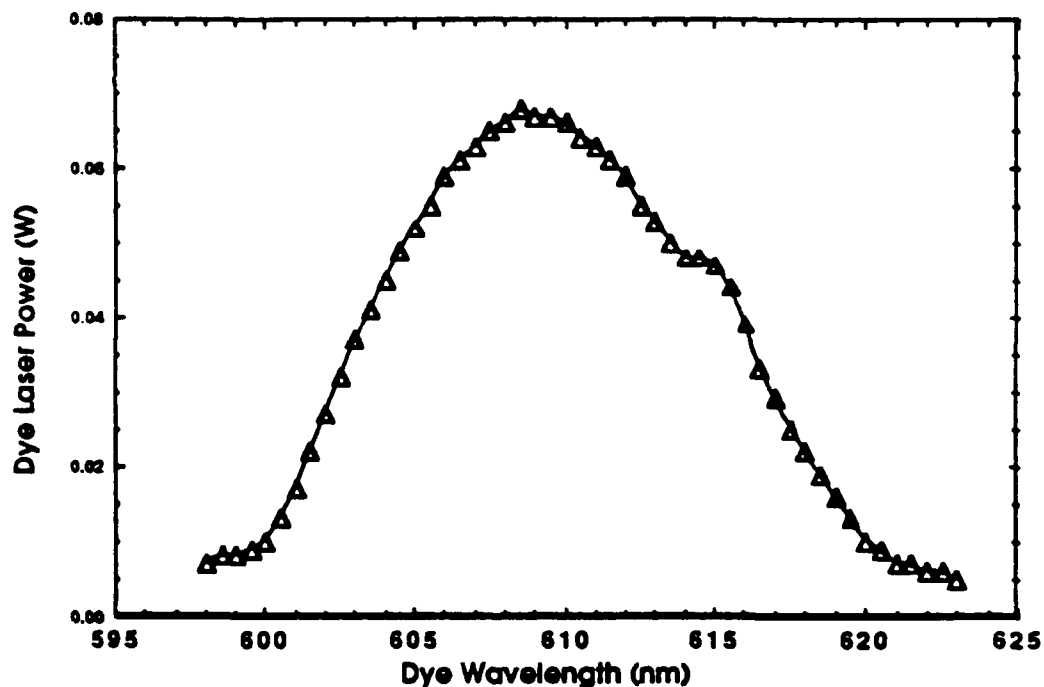


Figure 11. A typical power curve of the HyperDye 300 laser using Sulforhodamine 640.

The discharge chamber, shown in Figure 12, consisted of a 9-cm-diameter glass enclosure, Figure 12(a), two solid aluminum end plates Figure 12(c) and two molyb-

denum electrodes. The main glass enclosure had two tubular extensions for optical entrance ports. The quartz windows used on these ports were mounted at the Brewster's angle to reduce losses at the air-glass interface. These windows are approximately 19 cm from the center of the chamber in order to reduce the amount of energy deposited on the windows by the focused laser beams. The aluminum end plates hold the micrometers used for axial translation of the electrodes and provide the

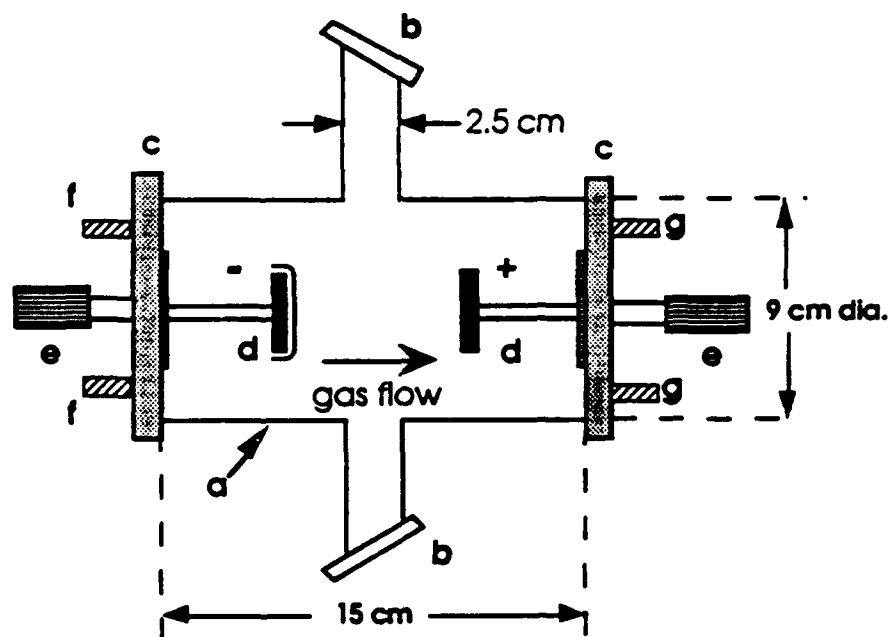


Figure 12. Diagram of the discharge chamber.

- a) Main glass enclosure.
- b) Glass tube extensions with quartz windows at Brewster's angle.
- c) Solid aluminum end plates.
- d) Molybdenum electrodes (Macor cap on cathode).
- e) Micrometer mounts.
- f) Gas inlet ports.
- g) Vacuum ports.

necessary support for the gas flow inlets and vacuum ports. The electrodes were molybdenum 5 cm in diameter. The cathode was covered by a Macor cap with a 9-mm-diameter aperture in the center to help stabilize the discharge at low operating currents.

### Optogalvanic Setup

The analysis of the HyperDye 300 scanning dye laser was carried out using the optogalvanic effect described in Chapter II. Figure 13 shows the optical system used for the measurements.

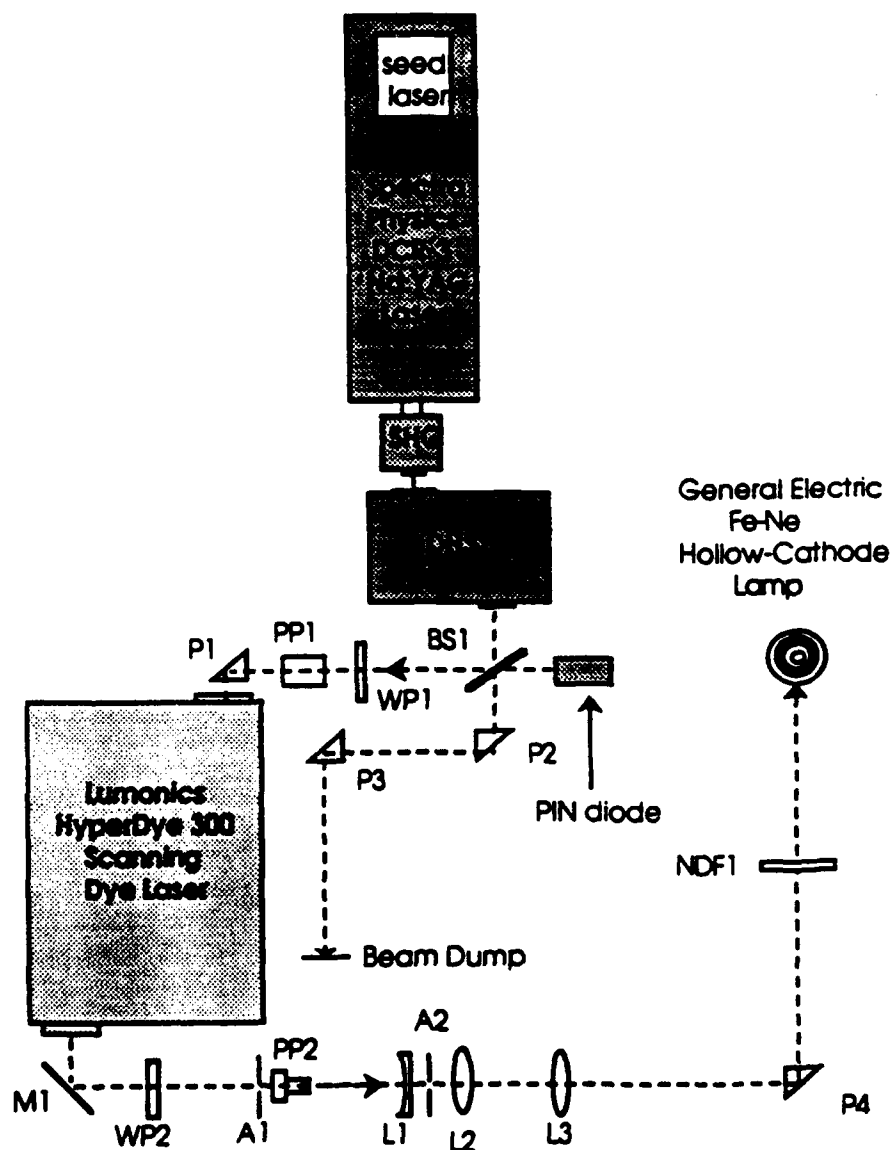


Figure 13. Optical system for optogalvanic measurements.

The optical layout for the OGE experiment used only the dye laser optics of the CARS system. Here, the dye beam was focused inside the hollow-cathode lamp very

near the surface of the cathode. The beam was focused by a 500 mm lens (L3) and was attenuated by neutral density filters (NDF1). Attenuation of the dye beam was necessary so that the OGE signal did not saturate and the laser did not damage the windows of the OGE cell. The neutral density filters were calibrated by measuring the intensity of the Nd:YAG beam before and after the filter and determining the transmission of the filter. This was important in light of the fact that the OGE signal changes drastically as the laser intensity is increased. Much of the time for this experiment was devoted to determining at exactly what point the signal saturated.

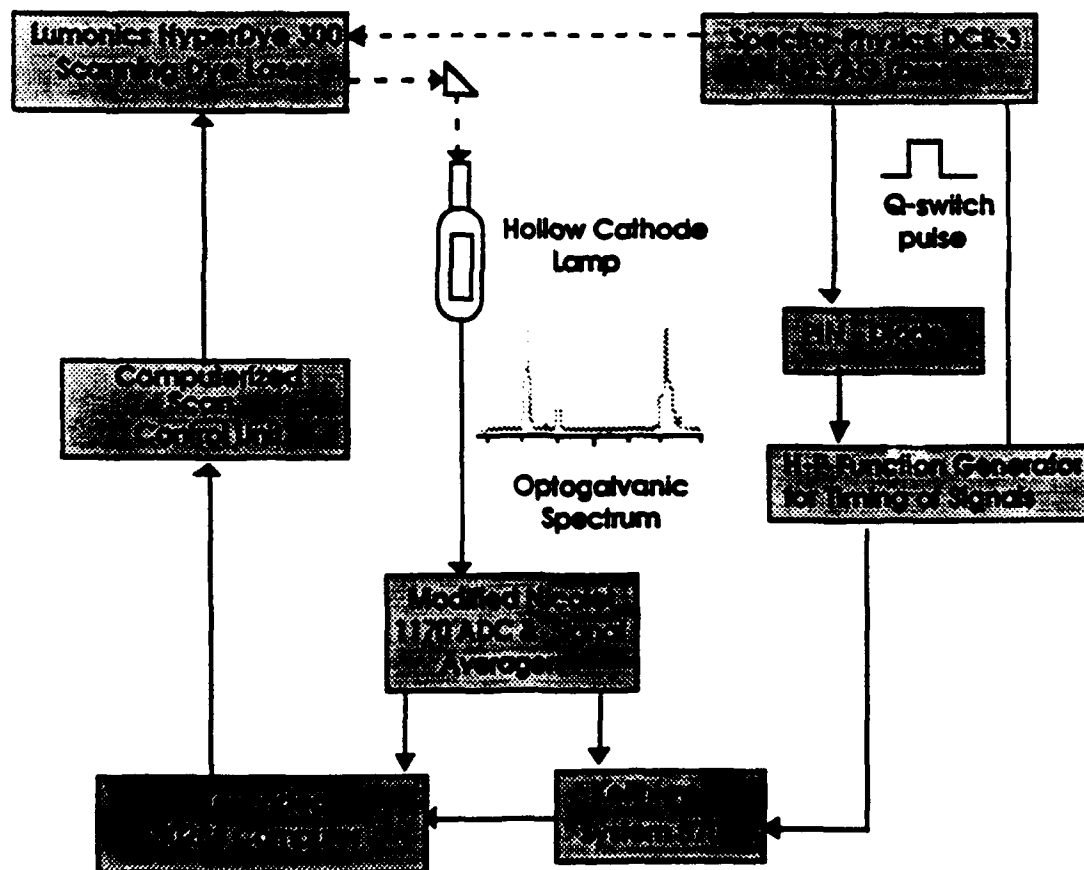


Figure 14. Data acquisition system for OGE experiment.

The data acquisition system for the OGE measurements, shown in Figure 14, was greatly simplified by the fact that the signal is a change in impedance. It was only

necessary to measure and record the voltage pulses across the lamp electrodes. The signal was fed directly into the Nicolet signal averager for digitization and storage. As with the CARS system, stepping of the dye laser grating was controlled by the Keithley unit and the Televideo computer. The timing of the signal was carried out using the Q-switch triggered PIN diode and the H-P Function Generator. After a complete spectrum was taken, the data was down loaded to the computer for analysis. The actual circuit used to obtain the OGE pulse given in Figure 15. The 180 pf capacitor provides a high pass filter with the equivalent circuit resistance and thereby passing only the OGE pulses.

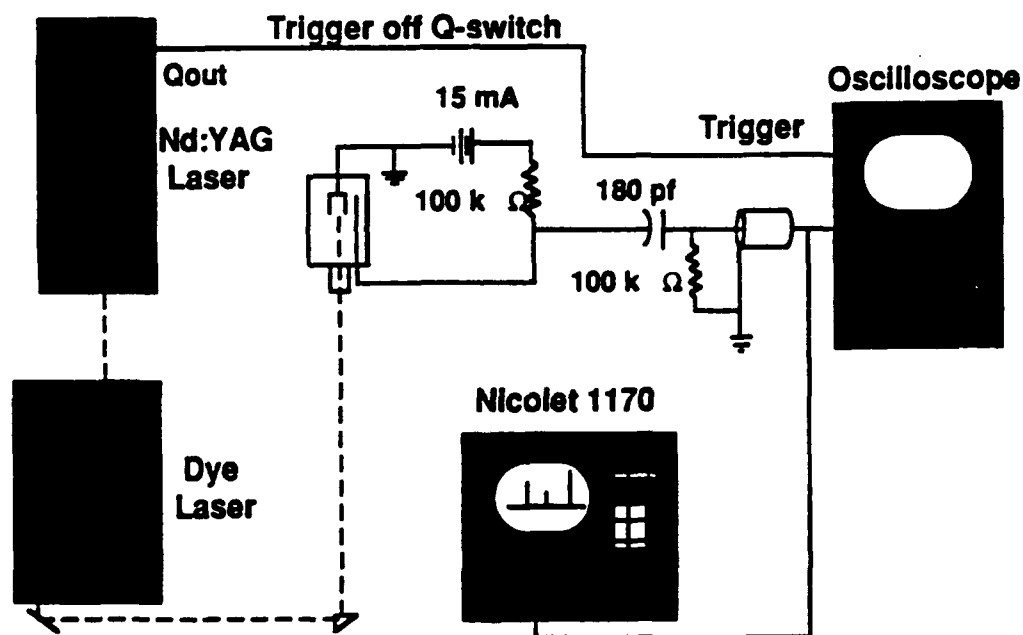


Figure 15. Circuit used to obtain OGE signal.

## CHAPTER IV

### DATA AND ANALYSIS I

In this chapter, results of experiments on the CARS system are presented. Optogalvanic measurements were made of the spectral line shape and absolute laser wavelength of the HyperDye 300 dye probe laser using an iron-neon hollow-cathode discharge lamp. These values were then evaluated in the CARS computer fitting procedure. The stability of the nitrogen discharge was also studied in order to determine the conditions under which the discharge remained stable for an extended period. Instabilities were observed visually, in the CARS signal and in the electrode voltage.

#### Motivation

The work done by Epling and Yaney<sup>5</sup> and Cirillo and Yaney<sup>6</sup> on both the CARS system and the discharge showed a need for two things. First, the Gaussian profile used for the probe laser lineshape used by Cirillo and Yaney in the fitting code showed a persistent mismatch from the lineshape observed. Thus, the actual lineshape was needed to improve the fitting of the data. Secondly, although a great deal of work was done by these workers in determining the stability conditions for their discharges, it became obvious that more work was needed. Both visual and spectral data showed evidence of instability in the discharge under the conditions imposed in the previous studies. This instability cast some doubt on the accuracy of the previous data and suggested that more data was needed to fully characterize a stable discharge. The discharge conditions used by Epling and Yaney and Cirillo and Yaney are given as Tables 2 and 3.

Table 2. Epling and Yaney's Discharge Conditions.

Electrodes:	Nickel-Iron Doorknob and glass caps
Current	= 60 mA
Current Density	= 0.09 A/cm <sup>2</sup>
Voltage	= 445 V
Total Pressure	= 31 and 40 Torr
Electrode Spacing	= 14mm
Flow rate (Nitrogen)	= 10 to 63 sccm
Flow rate (Argon)	= 0 to 200 sccm

Table 3. Cirillo and Yaney's Discharge Conditions.

Electrodes:	Flat Molybdenum & Macor Cap (Cathode)
Current	= 30 mA
Current Density	= 0.045 A/cm <sup>2</sup>
Voltage	= 540 V
Total Pressure	= 30 Torr
Electrode Spacing	= 14mm
Flow rate (Nitrogen)	= 85 sccm

The discharge device used by Epling and Yaney differed from that of Cirillo and Yaney and the work presented here in the type of electrodes used. The nickel-iron doorknob electrodes with apertured glass caps did not provide a stable nitrogen discharge. Argon was added to the system in an attempt to spatially stabilize the discharge.<sup>5</sup> The problem of a spatially centered nitrogen discharge was solved by Cirillo and Yaney with the switch to plane parallel molybdenum electrodes with the cathode covered by an apertured ceramic cap to constrain the discharge at the surface of the cathode. Although the data taken by Epling and Yaney had other problems, clipping of the data by the spectrometer for example, their study of signal strength, and Cirillo and Yaney's subsequent work on the subject, was important to the studies presented here.

### Dye Laser Evaluation

The spectral lineshape generated by the CARS system is basically a convolution of the line shapes of the three laser beams, the lineshape of the Raman transition and the projection of the spectrometer slit onto the control volume. In the case of narrow band CARS, where the pumping Nd:YAG laser has a linewidth on the order of  $0.006 \text{ cm}^{-1}$ , the recorded spectral width will be dominated by the dye beam linewidth. For scanning CARS, rather than single-shot CARS where in the entire spectrum is obtained with a single pulse of the pump lasers, the slit function passes the entire CARS beam and thus makes no contribution to the observed width. Figure 16 shows a typical narrow band CARS spectrum.

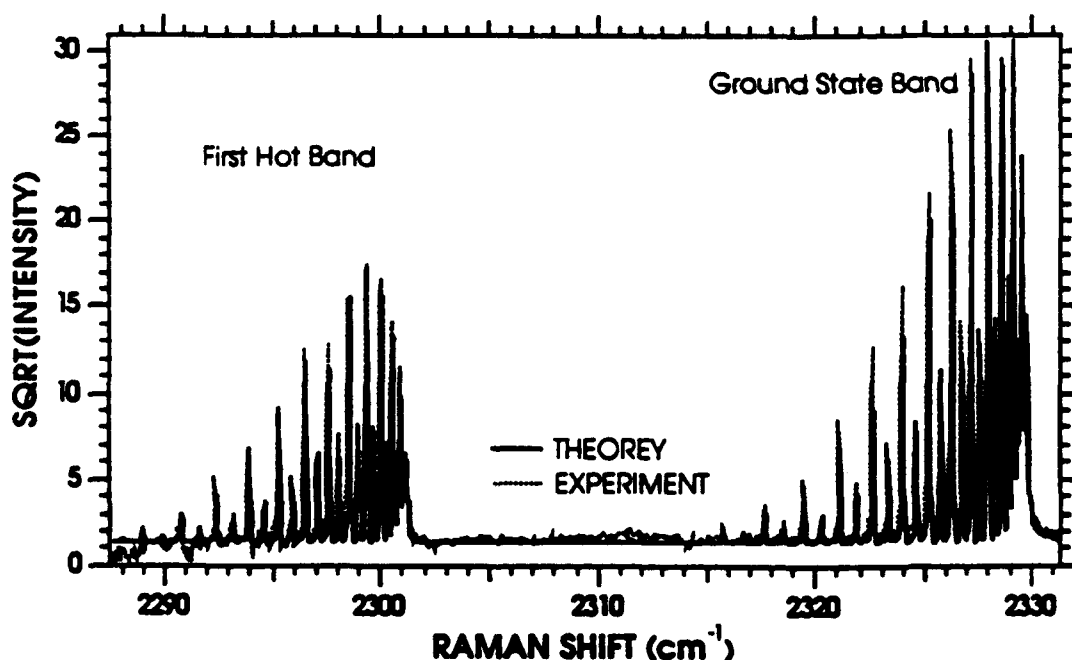


Figure 16. Typical narrow band CARS spectrum.

Figure 17, shows an expanded portion of the CARS spectrum of Figure 16, obtained in the narrow band mode, and the computer fit for the same spectrum assuming a Gaussian profile for the probe lineshape. It can be seen that at lower J



values (higher Raman shift), where the lines become less and less resolved, the Gaussian line shape is not in good agreement with experiment. The area at the base of each line is filled in more in the experimental data than in the theoretical spectrum. This observed behavior of these experimental spectra suggested that the experimental line shape has larger "wings", i.e. the profile goes to zero further from the peak than a normal Gaussian profile, and that the experimental profile was asymmetric.

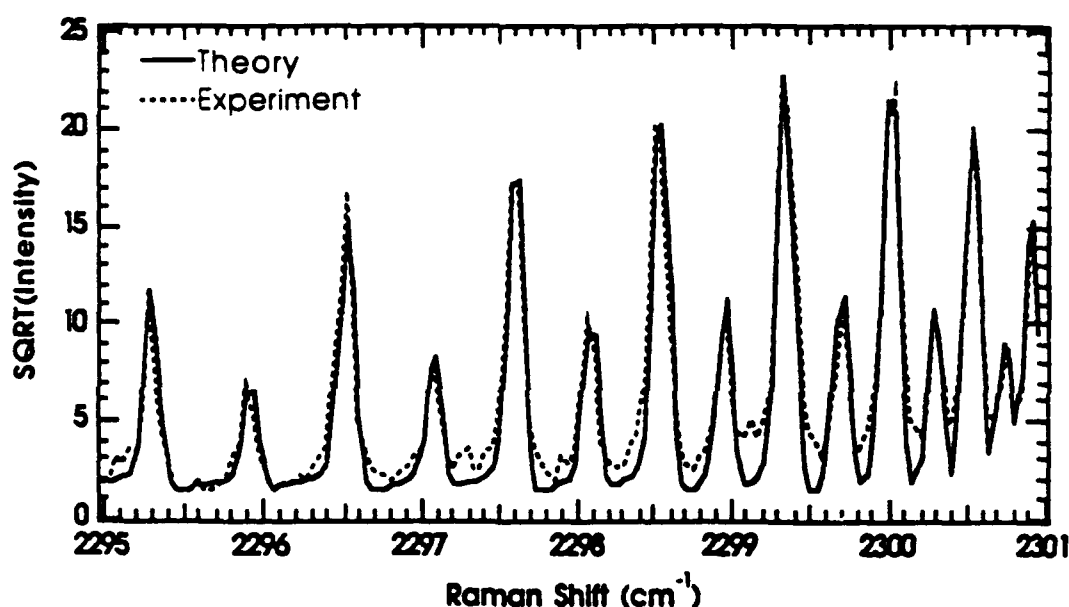


Figure 17. Expanded section of higher J lines in a typical spectrum.

In order to determine the actual line shape produced by the HyperDye 300 Laser, and to determine under what conditions the laser works best, the laser line was scanned using the OGE. The experimental procedure and setup described in Chapter III was used to obtain several spectra under varying conditions.

OGE spectra were taken of the 607.564 nm neon line, at differing pump powers, using the iron-neon hollow cathode lamp described in Chapter II. Typical spectra, given in Figure 18, show a strong dependence of the lineshape, both the width and symmetry, on the power of the incident laser. As the laser power decreased, the line went from a broad, asymmetric shape with very little extension on the wings, to a narrow, nearly

symmetric shape with very extended wings. The linewidth (FWHM) of the spectra narrows from  $>0.1 \text{ cm}^{-1}$  at  $14 \text{ } \mu\text{W}$  to a roughly constant value of  $0.07 \text{ cm}^{-1}$   $5.5 \text{ } \mu\text{W}$ . The peak of the line at the highest pump power can also be seen to flatten out. Coupled with the fact that the line width becomes constant at lower power indicates that the primary broadening mechanism of the OGE signal is that of power broadening.

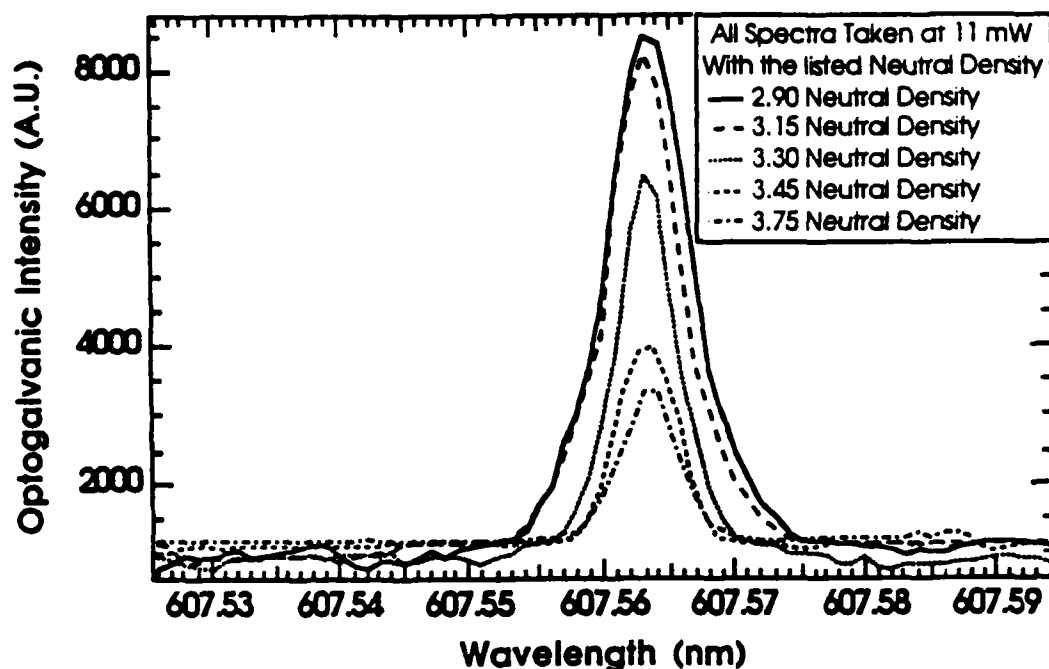


Figure 18. Line shapes observed using the optogalvanic effect on the dye laser. Neutral density filters were placed in the dye beam to control the power.

From Eq. (19), the Doppler width (FWHM) of the neon line at 900 K is  $0.003 \text{ cm}^{-1}$  (93 Mhz). Assuming that the laser line shape is roughly Gaussian, and using the fact that the square of the width of the convolution of two Gaussians goes as the sum of the squares, we can assume that the width of the transition does not effect the measured line shape.

$$\begin{aligned}\Delta v_{\text{meas.}}^2 &= \Delta v_D^2 + \Delta v_{\text{LASER}}^2 \\ \Delta v_{\text{LASER}}^2 &= (0.07 \text{ cm}^{-1})^2 - (0.003 \text{ cm}^{-1})^2 \\ \therefore \Delta v_{\text{LASER}} &= 0.07 \text{ cm}^{-1}\end{aligned}$$

The result of this work was the development of three lineshape spectra shown in Figure

19 from three of the profiles shown in Figure 18. These spectra provided probe files for use with the CARS fitting routine obtained from R. Palmer of the Sandia National Laboratory at Livermore, California.

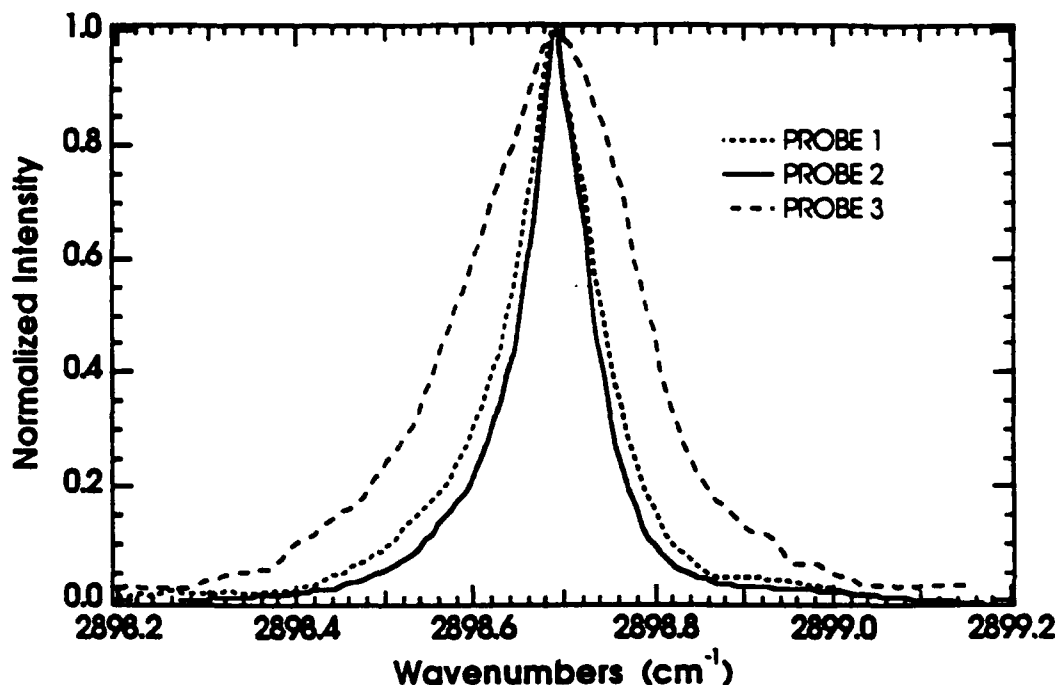


Figure 19. Probe files for use with the Sandia CARS fitting code.

The program has a built in Gaussian line shape function for the probe laser and can facilitate a user defined lineshape function. After preparing the lineshapes of Figure 18 for use in the program, several refits of old data were performed as well as fits to new narrow band CARS spectra. Figure 20 shows refits of the data from Figures 18 with the new probe line shapes. It is easy to see that both Probe 1 and Probe 2 gave considerably better results than that of Probe 3. This, taken with other refits of Cirillo and Yaney's data, show that the Gaussian profile assumed by the CARS fitting routine is not the lineshape of the dye laser. Probe 2 gave the best fit of the new lineshape to the data, and a refit of the CARS data shows only a small change (50 K - 75 K) in vibrational temperature and virtually no change in rotational temperature.

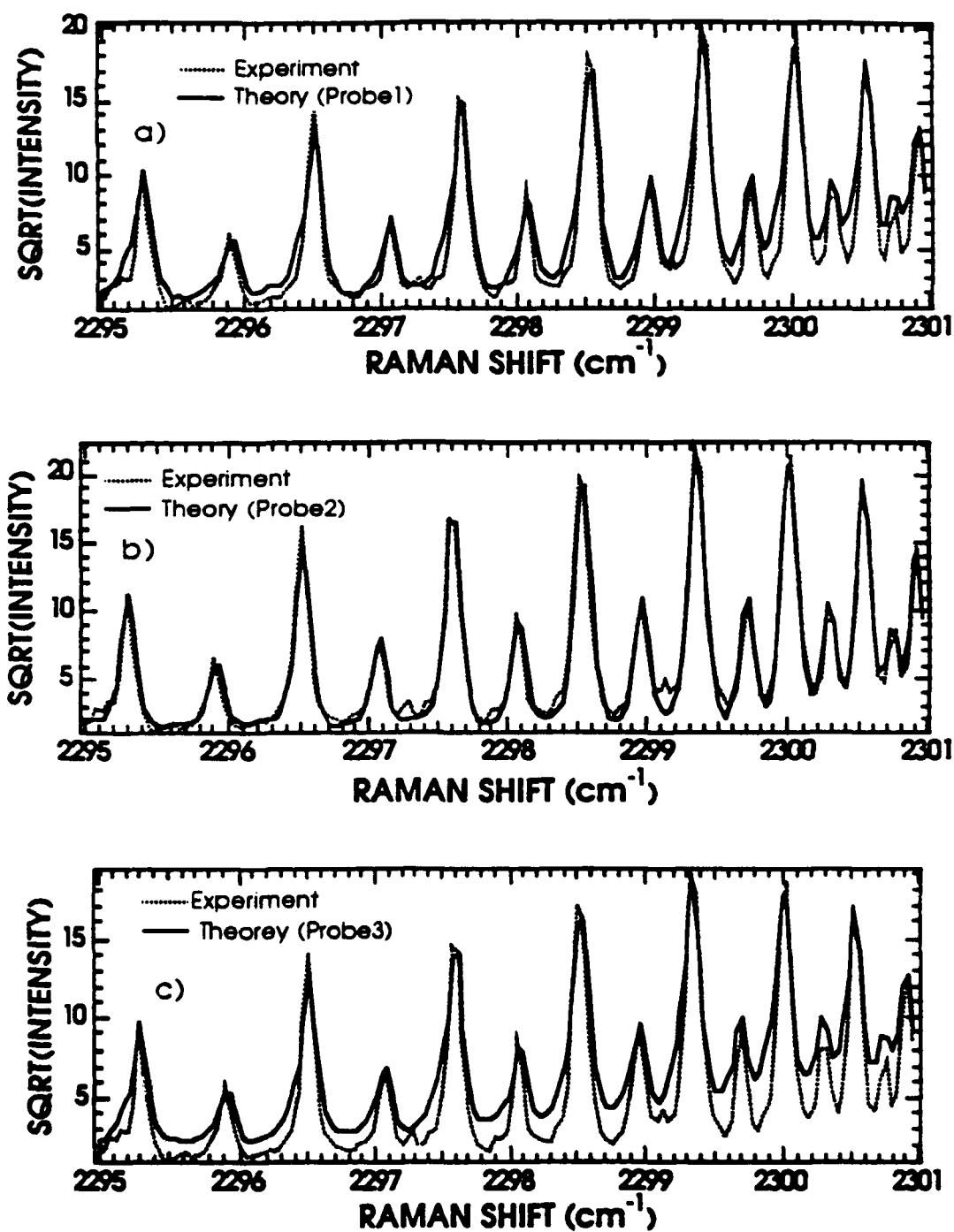


Figure 20. Refits of the data from Figures 17.

- a) Fitted using Probe 1.dat
- b) Fitted using Probe 2.dat
- c) Fitted using Probe 3.dat

After the work shown above, the system was modified to give greater control of the laser intensity. This was done by controlling the pumping of the dye by means of a polarizing prism, PP1 in Figure 9, and rotating the wave plate, WP1. When the wave plate polarization is aligned with that of the polarizing crystal, maximum pumping was allowed. Previous to the introduction of the laser polarizer, the output power of the dye laser was controlled by rotating the wave plate WP2. Because the dye laser is capable of very high intensities ( $> 80$  mW), but the CARS system operates at approximately 25 mW to avoid saturation,<sup>6</sup> this reduction of pump power does not present a problem. The side effect of this has been to improve the efficiency of the dye system and to reduce the amount of light "thrown out" by the wave plate WP2, thus optimizing the use of the dye beam and reducing the strain on the dye and extending its useful lifetime.

#### Discharge Instability

The amount of time required to obtain a single CARS spectrum, nominally 20 minutes without the seeder and one hour with, means that the discharge under study must be stable over at least that amount of time. On several occasions it was noticed that the discharge formed several distinct modes in the positive column and corresponding spots on the surface of the uncapped anode. The phenomena had been noticed by Cirillo and Yaney,<sup>6</sup> but not by any of the previous researchers, therefore it was determined that this instability was a product of the new electrode configuration implemented by Cirillo and Yaney. This was eventually seen as a possible cause of the "jumps" in the axial profiles of the measured vibrational temperature. This observation prompted the search to see if the instability was more general and could be observed in the CARS signal when the discharge appeared visibly stable.

Several experiments were carried out to characterize the instability of the discharge. First, the current to the discharge chamber was varied and the raw CARS

signals were recorded by Dr. Yaney. Secondly, a detailed visual study of the formation of the spots in the discharge was carried out by varying the supply current to the discharge chamber, recording the chamber voltage and photographing the spots.

To look at the CARS signal versus the supply current, a discharge was struck and the maximum of the ground and first hot state band were measured as the voltage across the discharge was varied by changing the supply current.<sup>27</sup> Figure 21 shows the changes in the ground state band signal. As can be seen, there is a splitting of the data. In order to see how this effects the vibrational temperature, Figure 22 shows the square root of the ratio of the hot band signal to the ground state band signal. The vibrational temperature is directly proportional to this ratio, within the range of these measurements. These data give clear evidence that the vibrational temperature was affected by some instability.

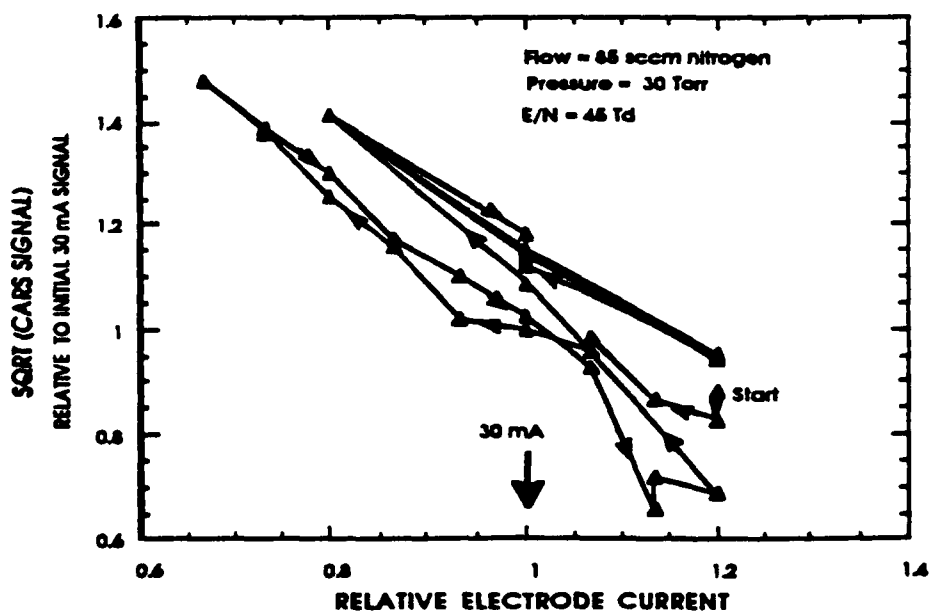


Figure 21. The square root of CARS signal (ground state) versus the supply current. The data shows a definite bifurcation of the CARS signal.<sup>28</sup>

The voltage across the discharge was also measured as a function of the supply current. A hysteresis effect in the voltage can be seen in Figure 23. As the current is raised from its initial value, the voltage drops roughly exponentially. When the current is

then lowered from this high value, the voltage remains nearly fixed over a large current range before rising very sharply near the lowest current at which the discharge can sustain itself.

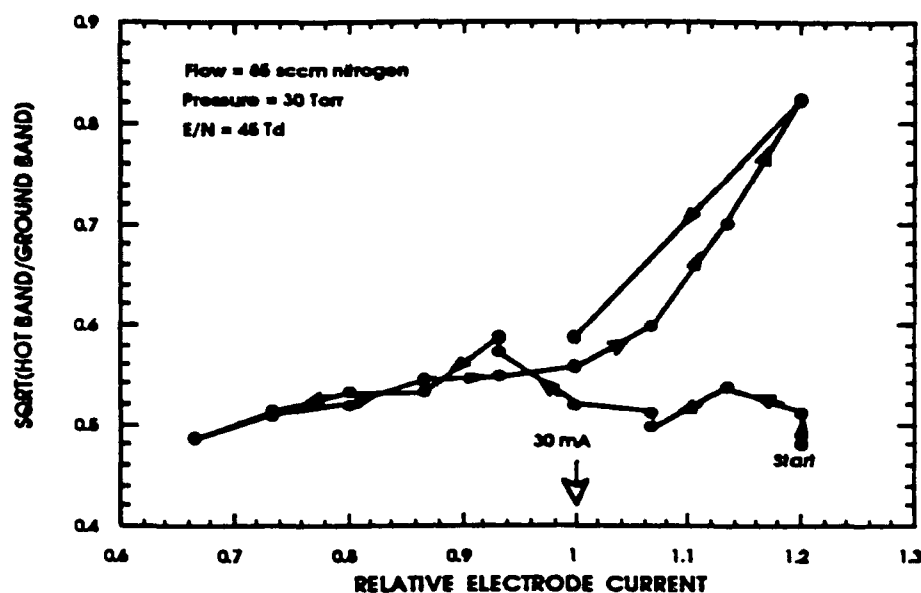


Figure 22. Square root of the ratio of the hot band and ground state (proportional to  $T_v$ ), showing the dependence of  $T_v$  on supply current.<sup>28</sup>

The general shape of the curves can be explained as a breakdown process by looking at the relationship between the supply current and the chamber voltage. At low current, the number of electrons being produced at the surface of the cathode is not large enough to overcome the resistance of the gas. As the current reaches some critical value ( $\sim 8$  mA here), the resistance of the gas is overcome by a few energetic electrons and a small current is generated in the gas. At this point a discharge is struck between the electrodes. As the electrons begin to flow, the gas temperature begins to rise from molecule-electron collision. This produces ions, these ions create more electrons in the gas, having the effect of making it easier for electrons to flow through the gas. The potential between the electrodes is reduced at the same time due to the increase of electrons reaching the anode. If the current direction is now reversed, the gas is in an highly ionized state, allowing electrons to flow through the gas easily over a

wide range of currents. Thus the potential across the electrodes stays relatively constant only rising near the critical current needed to keep the discharge going.

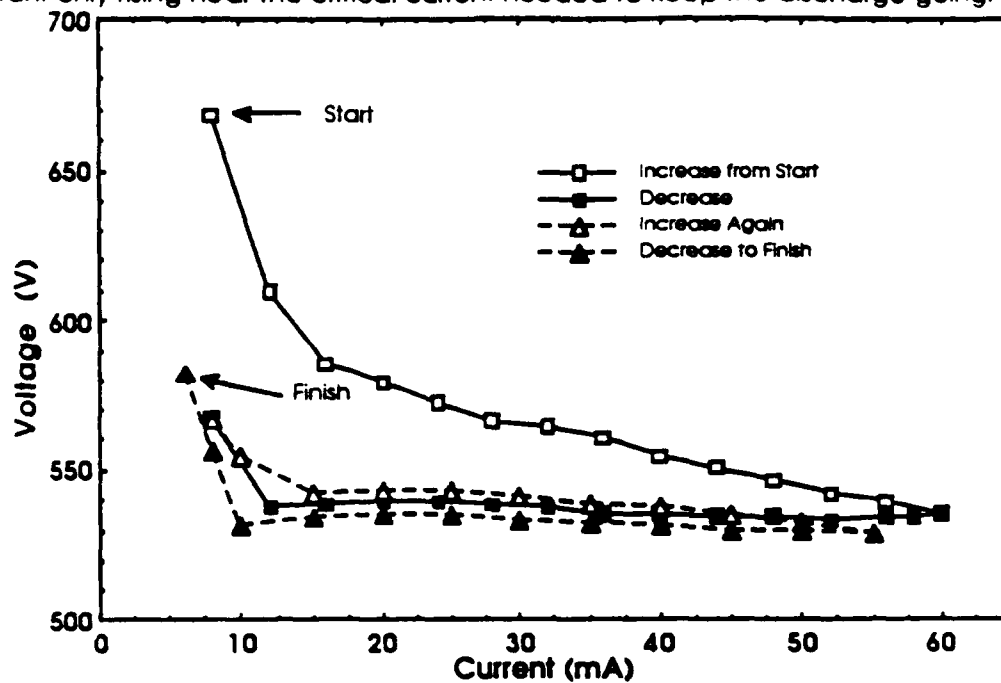


Figure 23. Data showing hysteresis of the voltage between the electrodes.<sup>28</sup>

The memory needed to explain the hysteresis comes from the gas. Although the gas is flowing, it has a residence time in the chamber on the order of minutes. Thus the gas in the chamber at the initially, remains in the system long enough to 'remember' the previous path it took on the V-I curve and follows the same path during repeated variation of the current.

This effect is further complicated by the cap over the cathode. The current needed to sustain the discharge must be offset by the current needed to just fill the aperture in the cap. Under filling the cap allows the discharge to wander around the exposed surface of the cathode. This type of instability causes a fluctuation in the voltage across the discharge. When the cap is overfilled, the opposite effect occurs. The current density at the surface of the cathode is such that the cathode glow is forced into the small aperture, generally causing the positive column to form a ring like pattern



and other non-visual instabilities in the discharge. These other instabilities show up in the voltage-current characteristics of the discharge seen above.

This instability induced in the voltage places some restrictions on how the experiment was carried out. First, because the voltage changes rapidly with minimal variation in current when going from low current to high current, and changes slowly over large variations in current in the opposite direction, the way in which the discharge is struck becomes an important factor. In general, the discharge is struck by raising the power supply voltage of the chamber until it is high enough to strike the discharge.

If the electrodes have begun to form a residue on the surface, further discussed below, the voltage needed to strike the discharge can be much larger than that with clean electrodes. Two types of film were noticed on the surface of the electrodes. First, in the center of the electrode where the discharge is located on the surface, a black colored residue forms on both electrodes with the cathode being much more affected. We believe this film is molybdenum nitride being sputtered onto the surface of the electrodes.

This film has the effect of changing the voltage-current characteristics of the discharge and to causes a splitting of the positive column. Normally the discharge strikes at a power supply voltage of around 2.1 kV for clean electrodes versus  $V_{PS} > 3.0$  kV for dirty electrodes. This translates to a power supply current of greater than 50 mA for dirty electrodes (depending on how dirty the electrodes are) versus  $I_{PS} \sim 20$  mA for clean electrodes. Thus the power supply voltage must be lowered to normal operating conditions. It is not uncommon to have to "fine tune" the current to make the cathode glow just fill the cap aperture as well, leaving the system in an unknown, possibly unstable, state. Normally the discharge is struck between the electrodes to the place on the surface of the electrode with the lowest work function, this is because electrons are easily released from these areas. Film on the surface of the electrode generally has

a higher work function than that of the surrounding area of relatively clean electrode and the discharge strikes to this area.

Because the discharge is not constrained at the surface of the anode, the positive column begins to wander from the center of the electrode in search of these areas of lower work function. Often this is seen as a wandering positive column or, at higher current, a splitting of the column. Figure 24 shows the dependency of the formation of these spots versus the applied electrode current,<sup>6</sup> and Figure 25 shows approximately what these patterns look like at the electrode surface.

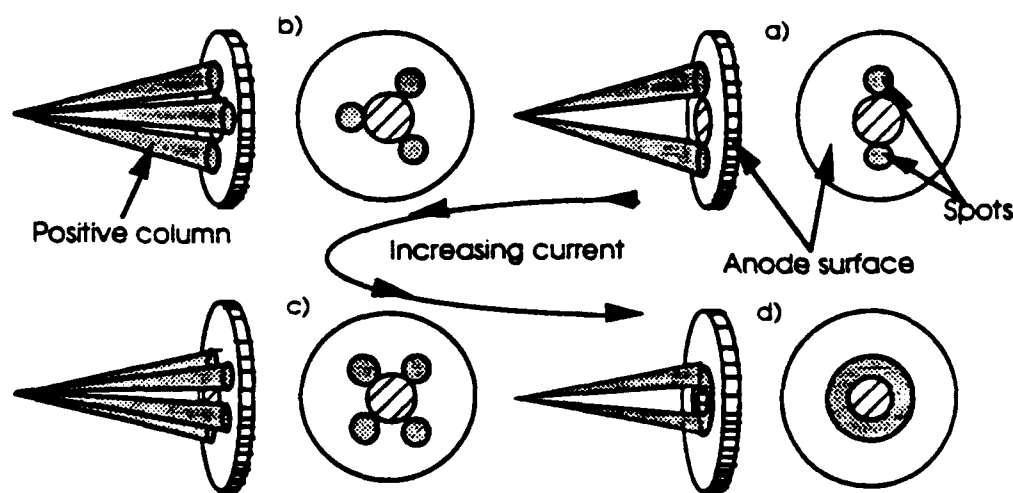


Figure 24. Multi-moding of the positive column and the pattern seen at the anode surface.

- a) Two spot pattern (~ 30 mA)
- b) Three spot pattern (~ 35 mA)
- c) Four spot pattern (~ 45 mA)
- d) Ring pattern (> 55 mA)

(The hatched area is that of the film, the shaded area is that of the positive column and spots visible on the surface of the anode. Often, the positive column is so faint that only the spots can be seen as an indication of the instability).<sup>28</sup>

The second type of film was observed on the anode only. A thin, gold colored film was noticed to build up over the entire surface of the electrode after the system had been in operation for long periods of time, greater than 5 hours. One possible explanation of this film is that of polymerization of contaminants in the system, possibly from the

gas or the silicon vacuum grease used to seal the chamber. This polymerization would be significantly enhanced by electron impact by the electrodes and contaminants in the gas. For an order of magnitude estimate of the amount of polymerization, assume that 10% of the electrons generated inside the discharge were striking the surface of the electrode. Assume as well that the number of electrons is roughly  $5 \times 10^{10} \text{ cm}^{-3}$  with a mean velocity between impacts of  $6 \times 10^6 \text{ cm/sec}$ . If these electron were incident on the face of the anode, the electron impact rate would be approximately  $10^{16}$  electron-s/sec for a period of  $2 \times 10^4$  seconds. Using an appropriate attachment rate for these electrons,<sup>29</sup> a rough estimate would be  $10^{15}$  atoms being deposited on the surface of the electrode during a nominal run time of 5 hours.

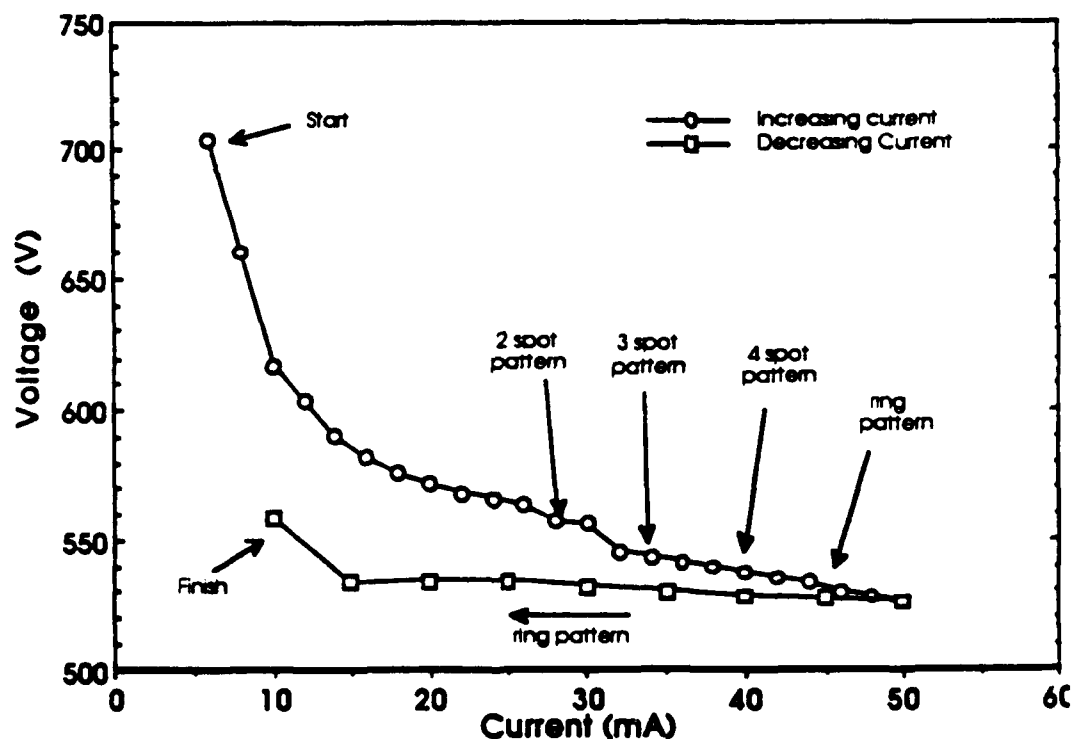


Figure 25. Spot formation as a function of applied electrode current at 30 Torr and 14 mm spacing.<sup>28</sup>

To become visible, the number of monolayers needed would be roughly 10. with  $10^{14}$  atoms per monolayer assuming the area of the electrode to be  $78 \text{ cm}^2$ . Thus,

even for this conservative estimate of electron impact, polymerization can be seen to be a factor on the conditions of the electrode surface. At the center of the electrode, i.e. on the axis of the discharge where the electrode surface may easily reach 500 K. At this temperature thermal effects enhance the polymerization of the electrode and indeed on the outer regions of the electrode, those near the edge, thermal polymerization would be the main effect because of the greatly reduced number of electrons in this area.

The surface of the cathode is not as effected by this polymerization because of sputtering of large molecules onto its surface. These heavy molecules, possibly molybdenum nitride, attach to the polymerized material and carries it away from the surface of the electrode.<sup>29</sup>

In order to counteract the effects of polymerization on the stability of the discharge, the electrodes were cleaned after each use. Cleaning was carried out in several steps. After being removed from the discharge chamber, the electrodes were polished in two steps to remove any foreign material from the surface. A large grit (0.5  $\mu\text{m}$ ) polishing material suspended in distilled water was used first. The electrodes were turned on a lathe while the polishing solution was applied to the surface with a damp sponge. The electrode was then rinsed with water and the process is repeated with a finer grit solution (0.05  $\mu\text{m}$ ) and a clean sponge to keep from scratching the surface of the electrode with any remaining 0.5  $\mu\text{m}$  particles. The electrodes were then rinsed with water and acetone to remove any large particles that may remain from the polishing. Finally, the electrodes were put in an ultrasonic cleaner while suspended in acetone to remove any remaining particles and water that may have built up during cleaning.

The Macor cap was cleaned with a pencil eraser to remove any deposited substances on the surface. It was then rinsed with distilled water and put in the ultrasonic cleaner. Special care was taken after cleaning had begun to ensure that the

electrodes were not touched by human hands. The organic material in the oil from the skin quickly etches into the surface of the electrode permanently damaging them.

## CHAPTER V

### DATA AND ANALYSIS II

Using the discharge conditions imposed by the stability studies presented in Chapter IV, CARS spectra were taken at four points along the discharge axis and at five radial positions, on axis and two on either side of the axis of the discharge. Computer fits of theoretical spectra to the experimental spectra were used to obtain rotational temperatures, vibrational temperatures and relative populations of neutral nitrogen in the discharge. Detailed analysis of the discharge is beyond the scope of this work, however, the approach needed to carry out such an analysis will be outlined and the mechanisms involved in producing the vibrationally excited nitrogen are studied.

#### Motivation

The data taken by Cirillo and Yaney,<sup>6</sup> Figure 26, showed a step in the axial profile of the vibrational temperature of approximately 300 K from 6 mm from the cathode to 8 mm from the cathode. The radial profile also showed a significant change in the vibrational temperature across the diameter of the discharge. The axial rotational temperature showed a slight, but continuous, drop from the cathode to the anode.

Since excited nitrogen can only decay to the ground state through collision, an attempt was made to explain the apparent drop in vibrational temperature by means of interaction between some collision partner and the vibrationally excited molecules. At a flow rate of 85 sccm, room temperature gas from the flow system had a velocity of approximately 0.22 cm/sec. This is far too slow to mix with the excited molecules fast enough or in such a small distance (2-3 mm) inside the discharge to act as a collision

partner causing such rapid excitation/de-excitation. Also, because of the large distance of the walls of the discharge chamber from the discharge itself, the walls of the chamber could not act as the third party. Any interaction with the walls of the chamber would also have a much more overall effect on the discharge as well. Indeed the work of Epling and Yaney<sup>5</sup> showed that the ground state band height increased smoothly as a function of radial position implying that de-excitation of the excited states, which lead to the increase in the height of the ground state band, is not a rapid process, but rather a slow one.

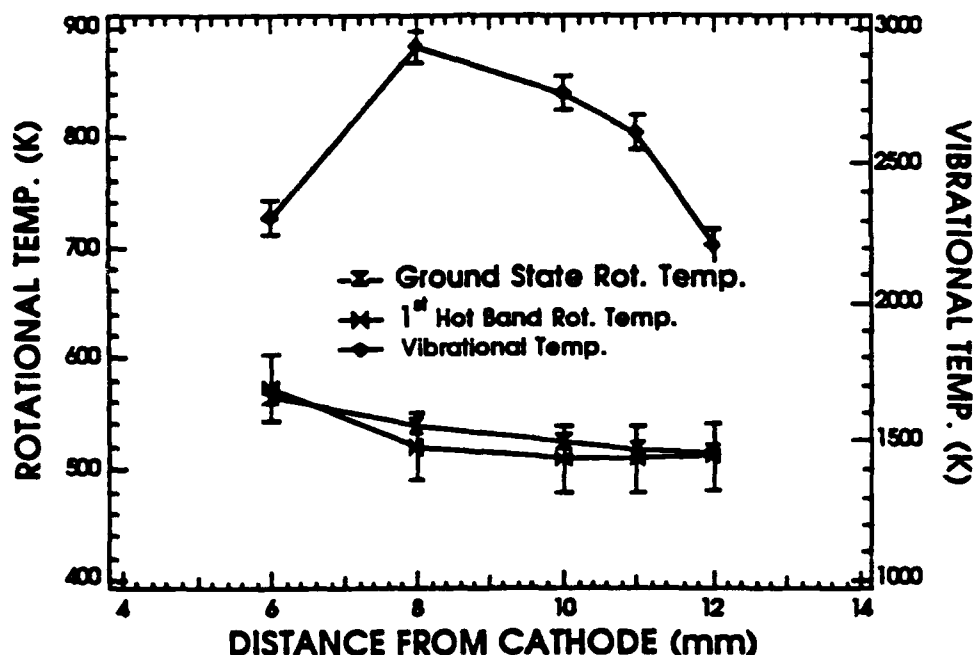


Figure 26. Axial temperature profile from Cirillo.<sup>6</sup>

#### New Experimental Data

Several attempts were made to repeat the axial data taken by Cirillo and Yaney in order to determine under what conditions the step in temperature were produced. While the new data did indeed show a similar step in temperature, Figures 27 and 28 are typical profiles of this effort, the discontinuity did not occur at the same position in the

discharge as that seen by Cirillo. In fact, the effect became worse. A sharp rise in the vibrational temperature was seen in the data at the edge of discharge near the cathode in the data taken on 10/25/90 in Figure 27 of more than 500 K. A similar rise in rotational temperature, which is fit independently for each vibrational band, can be seen in the Figure 28, but at the anode rather than the cathode here.

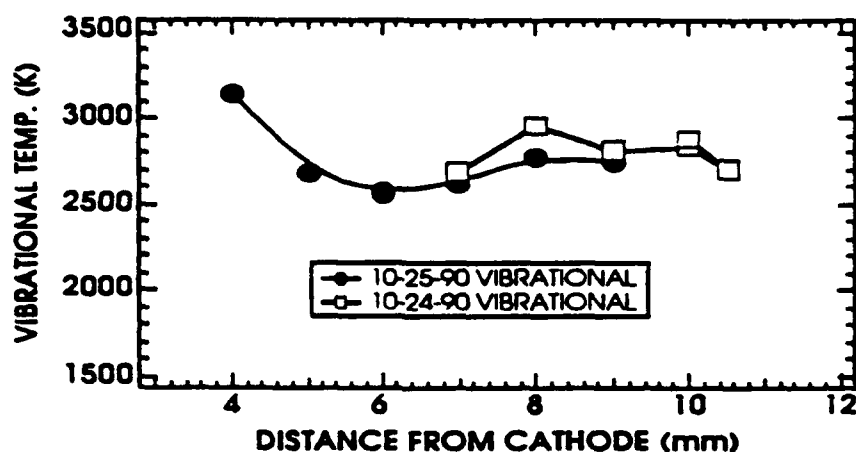


Figure 27. Vibrational temperature measurements centered on the region of the jump in Cirillo's data.

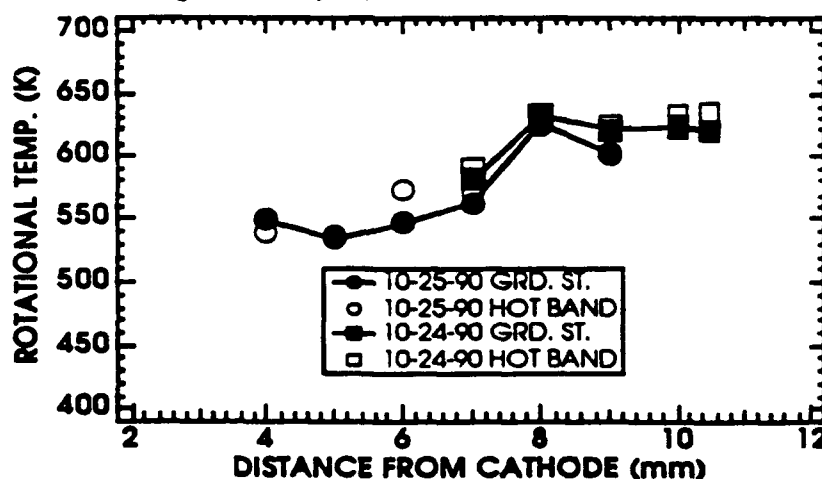


Figure 28. Corresponding rotational temperature profiles of Figure 27.

It was eventually considered that the cause of the step in the profile was not a discharge characteristic, but rather a systemic error introduced in some part of either the acquisition and/or the processing of the data. To study this possibility, several experimental parameters were determined to be possible sources of error: One, the



method of preparing the data for fitting. The problem of determining exactly where the background level of the system lies, i.e. what value should be subtracted from the measured signal in order to arrive at the proper signal level in the absence of this background. This can be a critical factor in the temperature fit to the data since after the background is subtracted, the square root of the resulting signal is used for fitting. The problem lies in the fact that the vibrational temperature is determined from the vibrational exponential factor in Eq. (15). The relative ratios of the heights of neighboring bands gives the exponential decay factor. The subtracted background can act as a bias either raising the temperature or lowering the temperature depending on whether or not too much or too little background is subtracted. The square root of the signal plus or minus some bias value does not equal the square root of the signal plus or minus the square root of the bias, i.e.

$$\sqrt{\text{bias} + \text{signal}} \neq \sqrt{\text{bias}} + \sqrt{\text{signal}}$$

The rotational temperature is also effected by this problem. The rotational temperature is fit to the data by fitting an exponential factor, the rotational exponential in Eq. (15), to the shape of the rotational lines inside a vibrational band. A bias factor here acts in the same way as with the vibrational temperature, but to a lesser degree.

This problem was partially solved by making several measurements of the background during a run by blocking the CARS beam and recording the zero signal level which was used as the background. Once a clear understanding of where the background was located, the spectra were prepared by subtracting a line fit to the measured background.

Secondly, adding to that of the background was that of a persistent problem with the Nicolet ADC and Signal Averager. At some points in a given spectrum, normally where the signal is relatively low, as happens between vibrational bands, the output signal of the Nicolet drops out. That is, the ADC losses track of the signal and does not

digitize the signal completely, reducing the signal to a low, although not necessarily zero, value for a short period of time before returning to the proper signal level. Because it was not always possible to tell if this had happened while taking the data, temperatures inconsistent with those measured elsewhere were often encountered. This was combated by visually inspecting the data sets and editing out these areas if possible, or inspecting the theoretical fits to the experimental data to see if there was a consistent mismatch that could be contributed to these dropouts. Often this error could be spotted when one part of a spectrum looked too low or too high when compared to other sections. When this occurred, it was generally left up to the person doing the fitting to "eyeball" the best fit. Spectra which were not consistent with others taken at the same location or near by were discarded.

Third, because dropouts and the relative noise level, which is amplified in the square root process, limit estimates of the value of the higher rotational lines ( $J > 28$ ), the computer code was modified by Dr. Yaney to exclude those values. This also improved the fitting speed. A single data set would normally take from 10 to 12 hours to fit, this time was cut to less than 8 hours. The vibrational temperature fitting error dropped as well, from 150 K to 200 K previous to this change, to an average of around 100 K.

None of the these possibilities produced a consistent temperature profile, although they did improve the precision of the temperatures fit to the data. The last possibility considered was that of the position of the center of the discharge relative to the control volume of the CARS system. Normally, after the system was aligned in room air to maximize the CARS signal, the discharge chamber was positioned in the path of the three beams and the center of the discharge was found by inspecting the reflection of the crossing pattern of the Nd:YAG beams on the surface of the anode. It was considered to be centered when the chamber was moved so that this crossing was in the center of the electrode.

It was found by Epling and Yaney that the height of the ground state band had a parabolic dependency on radial position, with the minimum occurring on axis.<sup>5</sup> Using this principle, measurements were made in the same way as before, only the discharge chamber was centered radially by moving the chamber until the ground state band was minimized both vertically and horizontally, transverse to the discharge axis. Figures 29 and 30 show that this solved the problem of the jump in temperature.

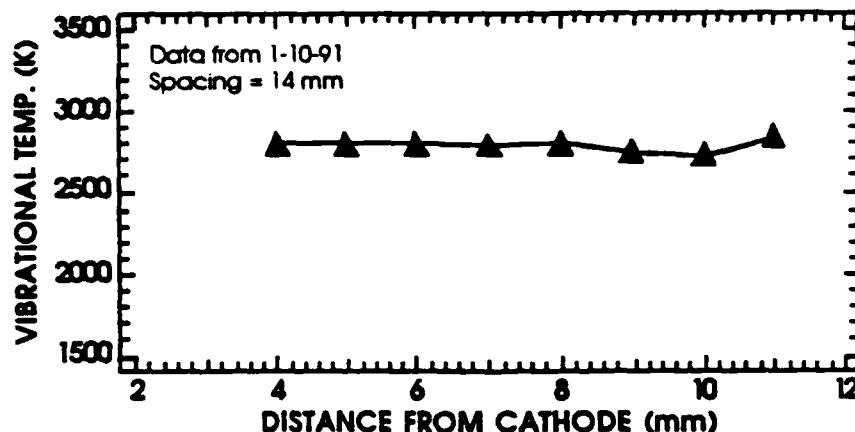


Figure 29. Vibrational temperature profile obtained after centering discharge at each axial position using the principle from Epling and Yaney.<sup>5</sup>

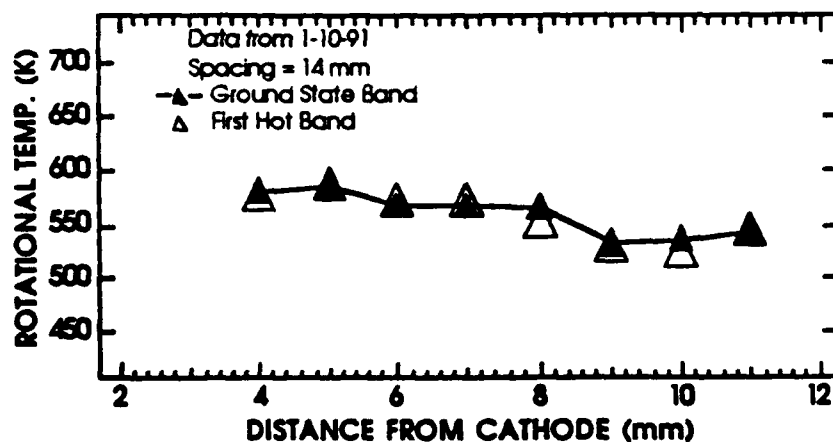


Figure 30. Rotational temperature profile from same data in Figure 29.

The rotational temperature profile can be explained as follows. The rotational temperature is in thermal equilibrium with the translational temperature and is affected by the cooling from the flowing gas and heating from the cathode cap. Because the

cathode is covered almost completely by a ceramic cap, it is expected to be somewhat hotter than the bulk of the discharge as the cap retains heat. Since the vibrational temperature is a measure of the density of low energy electrons and is not in thermal equilibrium with the translational temperature, it is not expected to be affected by the thermal gradient in the translational temperature.

The next step in characterizing the discharge was to measure the temperature profile of the entire discharge rather than simply on axis or radially at a single axial position. This required taking over twenty data sets. The amount of time to make these measurements in the narrow band mode of the CARS system would have been prohibitive, therefore the spatial profile measurements were taken in the broad band CARS mode. This reduced the time per spectrum from nearly an hour to just under half an hour, while not reducing the precision of the resulting temperatures appreciably.

Measurements were made at five radial locations: -6 mm and -3 mm from the center of the discharge, on axis and +3 mm and +6 mm from the center of the discharge, and at four axial locations: 4 mm, 6 mm, 8 mm and 10 mm from the cathode surface. Measurements at +6 mm and -6 mm were outside the visible boundary of the discharge and were intended to give an indication of how the discharge changed at the boundary. A slight miscalculation of the electrode spacing resulted in an electrode spacing of 12 mm rather than the 14 mm that had been used in the previous results. The only impact of this change was the reduction of the size of the positive column, and did not have any appreciable impact on the results of this experiment. A spacing of 12 mm was used for the remainder of the experiments presented here. Table 4 gives the discharge conditions used for the data plotted in Figures 29 and 30, while Table 5 gives the discharge conditions used in subsequent measurements.

Table 4. Discharge conditions used for data in Figure 29 and 30.

Electrodes:	Flat Molybdenum & Macor Cap (Cathode)
Current	= 20 mA
Current Density	= 47 mA/cm <sup>2</sup>
Voltage	= 540 V
Total Pressure	= 30 Torr
Electrode Spacing	= 14mm
Flow rate (Nitrogen)	= 85 sccm
E/N	= 45 Td

Table 5. Discharge conditions used in all measurements after the data of Figure 29 and 30.

Electrodes:	Flat Molybdenum & Macor Cap (Cathode)
Current	= 20 mA
Current Density	= 47 mA/cm <sup>2</sup>
Voltage	= 512 V
Total Pressure	= 30 Torr
Electrode Spacing	= 12mm
Flow rate (Nitrogen)	= 85 sccm*
E/N	= 52 Td

\* The flow rate was higher on 3/4/91 due to a blocked valve in the flow meter

A typical set of CARS spectra is given as Figure 31.

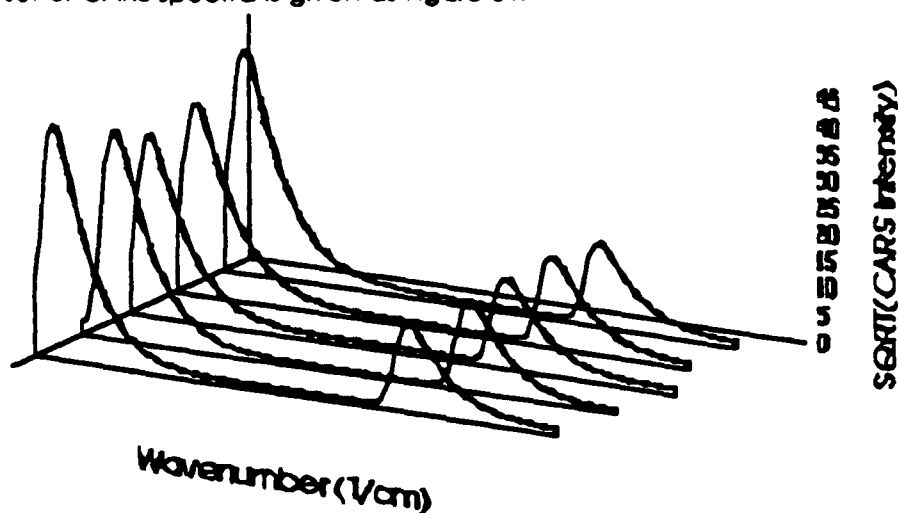


Figure 31. CARS spectra 8 mm from cathode. From the back, spectra are at the radial positions +6 mm, +3 mm, on axis, -3 mm and -6 mm.

The variation in the ground state band is on the order of 50% radially, while the first hot band shows at most a 1-2 % variation in the radial direction with the maximum

occurring on axis. As a check for consistency in the data from the two-dimensional study of the discharge versus the previous axial-only data in Figures 32 and 33 show the axial behavior of both the vibrational and rotational temperatures. The curves seen in Figure 32 are parabolic curve fits to the data and the curves in Figure 33 are linear fits to the data.

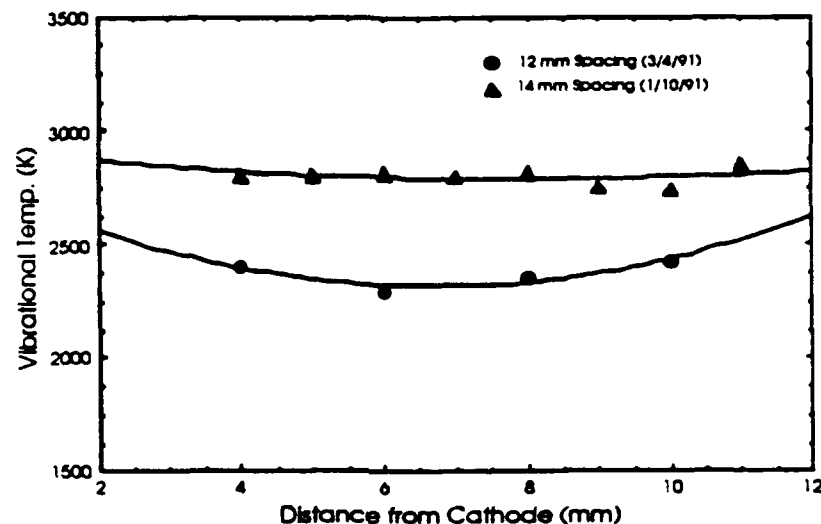


Figure 32. Comparison of 12 mm and 14 mm axial temperature profiles.<sup>31</sup>

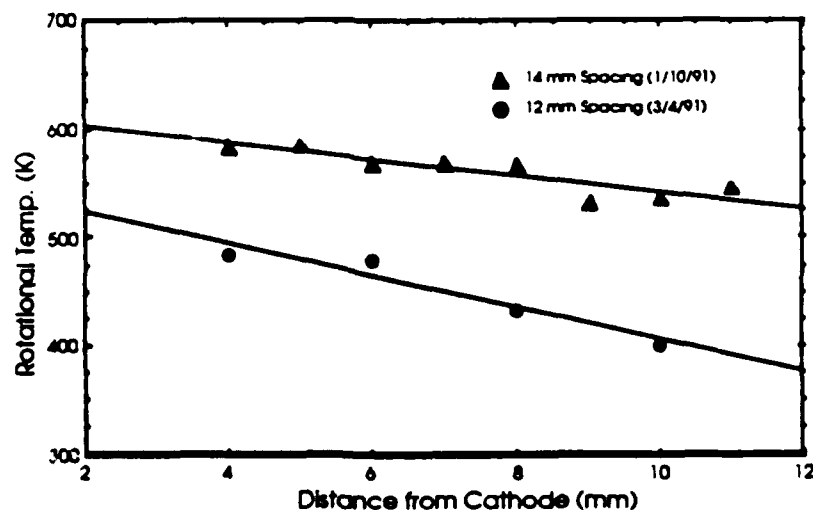


Figure 33. Rotational temperature comparison of 12 mm and 14 mm spacing.<sup>31</sup>

The two-dimensional vibrational temperature data is plotted in Figure 34. The data shows an interesting 'pinch' in the temperature at the center of the discharge, but

remains relatively flat across the length of the discharge. This pinch occurs at approximately the same location in the discharge as the tip of the positive column.<sup>31</sup> The rotational temperature profile, Figure 35, shows a thermal gradient from the cathode to the anode, and a small dip in temperature at one side. This dip is possibly caused by a local cooling due to the flowing gas, which enters the system from the cathode end of the chamber and flows around a splash plate to diffuse the gas as it enters the chamber. The actual gas flow pattern was not known.

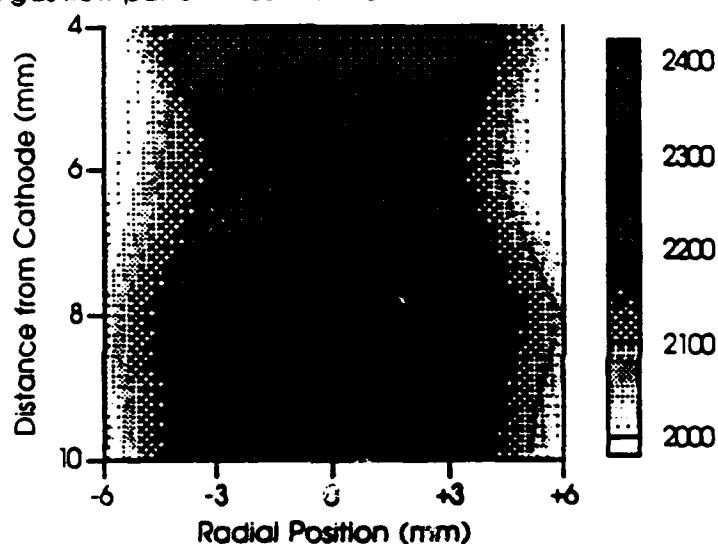


Figure 34. Vibrational temperature profile of discharge.

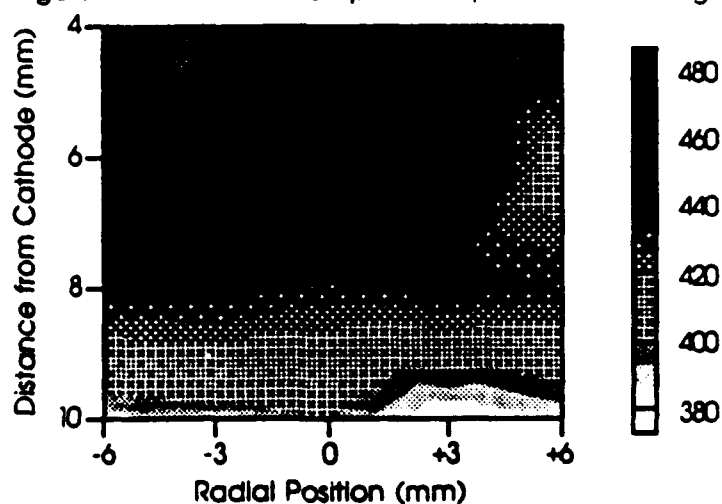


Figure 35. Rotational temperature profile of discharge.  
(The surface shown are a linear interpolation to the data points by DeltaGraph Ver. 1.1)

In an effort to understand the behavior of the first hot band relative to the ground state band, it was decided that spectra including the second hot band were necessary. Figure 36 shows these spectra and the vibrational and rotational temperature associated with them. Figures 37 and 38 give the radial temperature profiles.

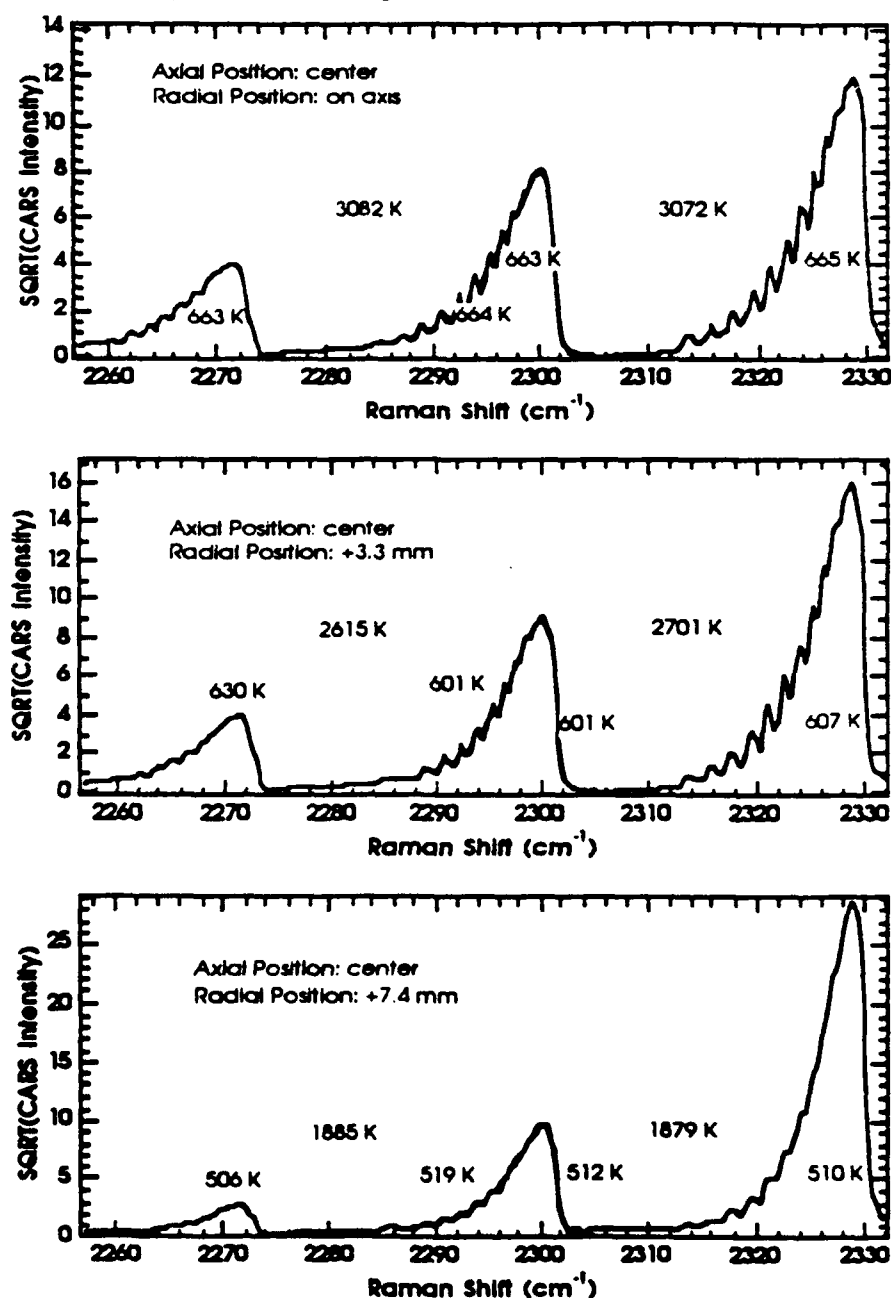


Figure 36. Measurement of the second hot band at three radial locations.



These measurements were made at a single axial location (6 mm from the cathode), and at three radial locations: the center of the discharge, 3.3 mm and 7.4 mm from the center.

The double temperatures of the first hot band are a result of the method by which these spectra were obtained. In one data run, the ground state and first hot band are measured together. In a second run, at the same location, the first and second hot bands are measured together. Theoretical spectra were then fit to both sets of data, the common link between the two being the first hot band. The first hot band acted as a scale between the two data sets, the first hot band/second hot band spectra were scaled until the first hot band was of equal size as the first hot band of the first hot band/ground state band spectra. The reason for the dual data sets was that the dynamic range of the electronics used was not sufficient to obtain both the large ground state band and the comparatively small second hot band with the same attenuation of the photomultiplier. The neutral density used to limit the amount of light arriving at the PMT was reduced from 24 to 8 in order to measure the second hot band while the PMT voltage was held constant.

It should be noted here that the distances over which we could make measurements was limited in the radial direction by the size and spacing of the entrance windows and by the electrodes in the axial direction. Since the laser beams interact at an angle, they are separated by approximately 5 mm at the face of the entrance windows limiting the vertical movement of the chamber to roughly 10 mm. The spacing of the windows also limits the longitudinal distance, along the direction of the laser beams, that the chamber may be moved. As the windows are moved closer to the focus of the laser beams, the energy density at the surface becomes high enough to burn holes in or crack the quartz.

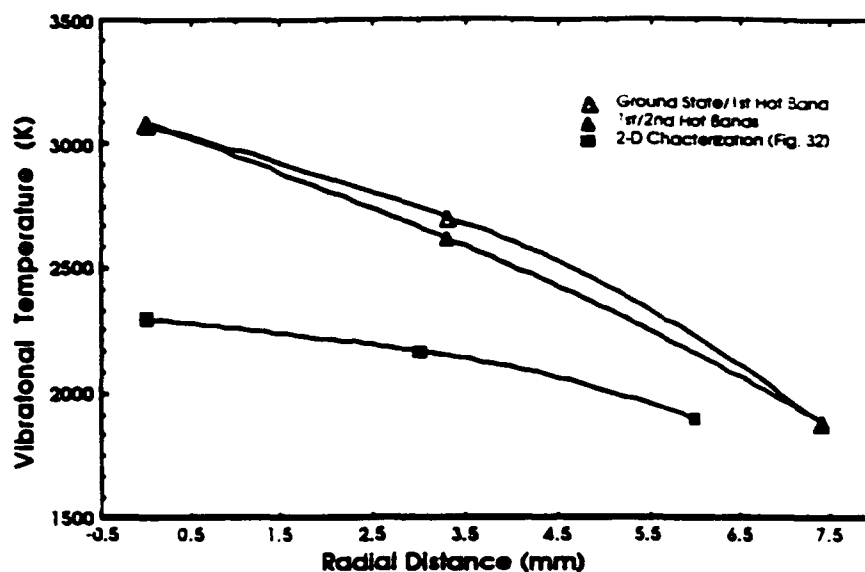


Figure 37. Comparison of radial vibrational profiles taken at the same axial location.

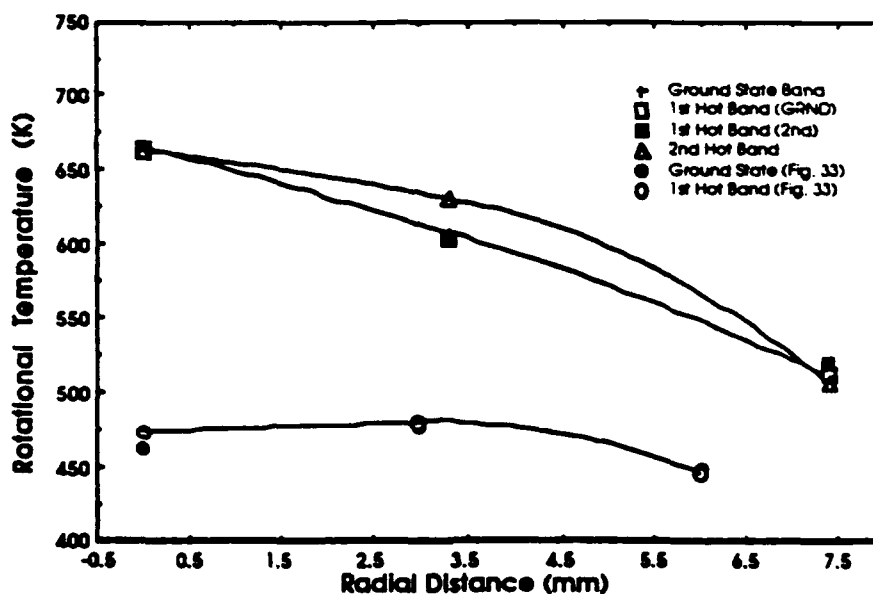


Figure 38. Comparison of radial rotational profiles taken at the same axial location. (GRND) means 1st hot band and ground state band data (2nd) means 1st hot band and 2nd hot band data.

As Figures 37 and 38 show, although the temperatures from the two sets of data are different, the general trend for both the rotational and vibrational temperatures are that of a smooth drop in temperature with increasing radius. It is postulated that the low temperatures measured during the two-dimensional discharge study in comparison to

those measured at other times, seen in Figures 30, 31, 35 and 36, were caused by a blockage in the mass flow meter used to monitor the flow rate. The flow meter is very sensitive to any contaminants in the gas such as dust particles, and in this case, we believe, measured a flow below that which was actually there. This has the effect of lowering the residence time of the molecules in the discharge region, thereby lowering the gas temperatures. This should not, however, degrade the usefulness of the data, rather it gives an indication of the conditions present in the discharge.

### Analysis of Data

Having obtained several sets of data which are both consistent with themselves as well as with each other, an order of magnitude calculation of some of the rates involved with the various primary excitation mechanisms will give an idea of how a more comprehensive analysis of the discharge data should proceed.

Figure 37 shows the variation of the height of the ground state band with respect to position in the discharge. Coupled with Figure 39, the variation of the height of the first hot band with respect to position, we can begin to see what mechanisms are responsible for the population of the differing bands, or rather, we can see that the mechanisms are not the same for the ground state band and, by inference from the second hot band measurements, the first and second hot bands. As we can see, the hot bands remain relatively constant over most of the discharge, the exception being near the cathode. As stated earlier, this can be attributed to the gas flow cooling the discharge at that location. The ground state band, however, changes by almost 60% from cathode to anode. Both bands definitely increase in height near the anode surface.

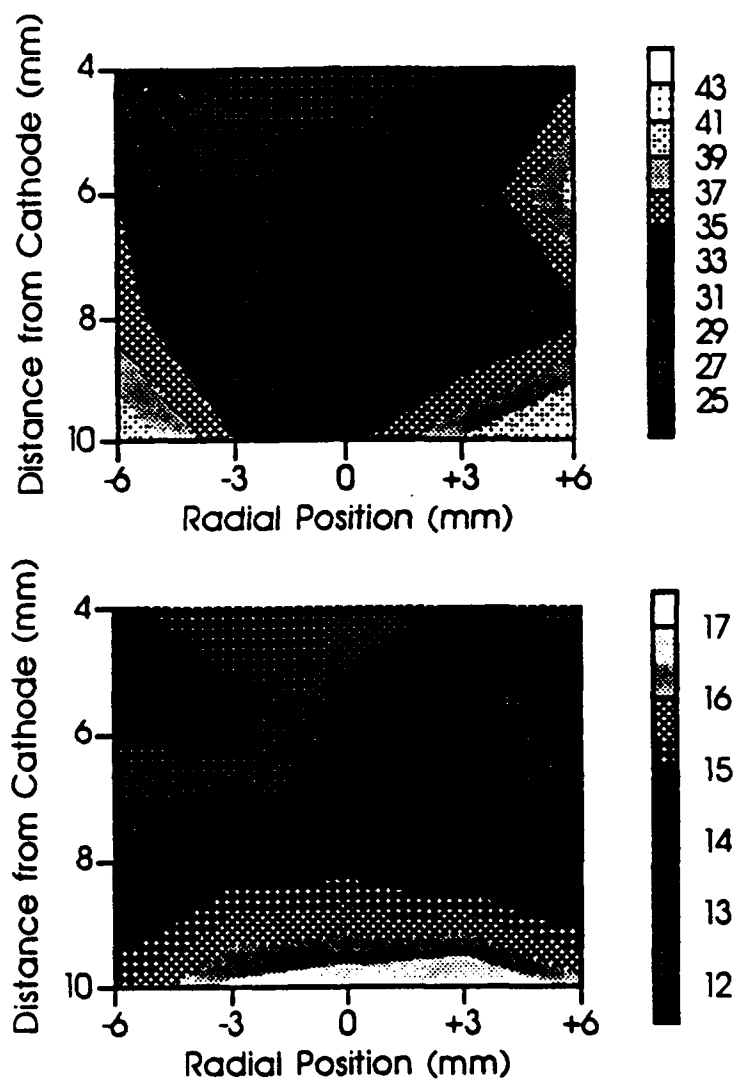


Figure 39. Two-dimensional representations of the ground state band signal (top) and the first hot band signal (bottom). The gray scale is the square root of the CARS signal at the maximum of the band.

To a first approximation, assume that the integrated signals in the bands are dominated by the number of molecules in the lower state. Then, the population difference is approximately equal to the lower state population and the population difference in Eq. (9) can be replaced by the lower state population. That is,

$$\begin{aligned}\Delta N &= N_0 - N_1 = N_0 \\ N_1 - N_2 &= N_1 \\ N_2 - N_3 &= N_2\end{aligned}$$

This means that the individual bands in Eq. (15) can be separately integrated over the rotational lines to obtain the total relative population in each vibrational state which can then be added to give the total number density. This density should then follow the ideal gas law,  $N_0 = p/k_bT$ . Typical spectra show that the ratio of  $N_1$  to  $N_0$  in the ground state band is on the order of 10% and the ratio of  $N_2$  to  $N_1$  in the first hot band is roughly 15%.

In Figure 40 the log total integrated areas under the curve in the three spectra of Figure 36 is plotted versus the inverse of the rotational temperature, or, as stated previously, the translational temperature. In this approximation, assuming an ideal gas law behavior, the total population under the curve show a linear dependency between the integrated signal (which is directly proportional to the population) and the inverse of the temperature.

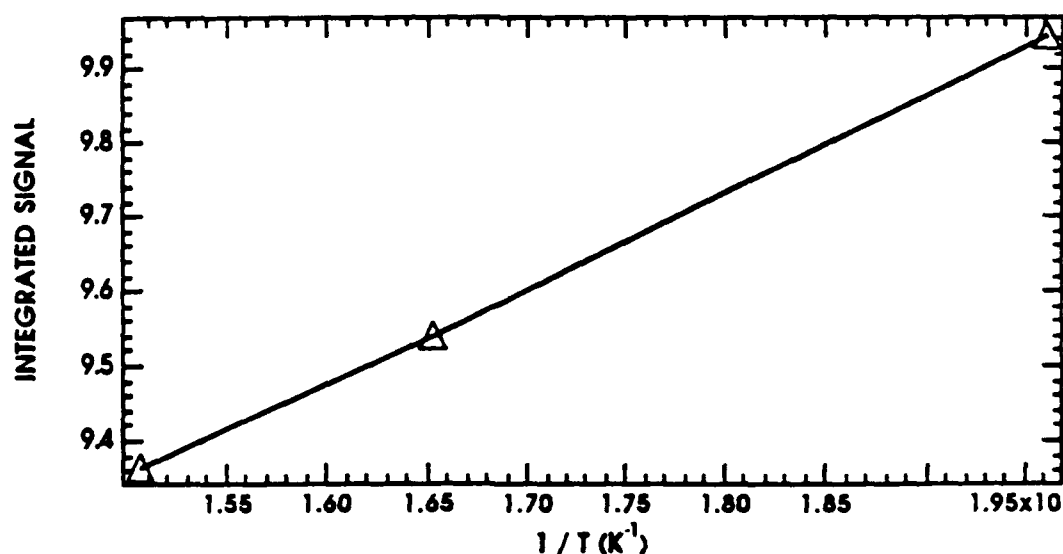


Figure 40. Integrated signal is proportional to the total population and shows a linear dependence on  $1/T_r$ .

Full analysis of the data requires the use of a set of rate equations which govern the number of molecules in a given vibrational excited state. A full rate equation model of the discharge is beyond the scope of this work, however the general type of analysis needed and a few examples of the change in the population into and out of the first

vibrational level is given below.

In order to gain some understanding of a few of the rates involved with the discharge, let us look at the pumping rates due to three of the main mechanisms for pumping of the  $v = 1$  vibrational level.

The master rate equation given by Capitelli, *et al.*,<sup>33</sup> is

$$\frac{dN_v}{dt} = \left(\frac{dN_v}{dt}\right)_{e-v} + \left(\frac{dN_v}{dt}\right)_{e-D} + \left(\frac{dN_v}{dt}\right)_{v-v} + \left(\frac{dN_v}{dt}\right)_{v-T} + \left(\frac{dN_v}{dt}\right)_{rec} \quad (21)$$

Where  $N_v$  is the population in the  $v^n$  energy level and the relaxation terms are:

- e-V = Vibrational excitation due to electron impact.
- e-D = Electron dissociation of the molecule (only in ground state).
- V-V = Exchange of energy between vibrationally excited molecules.
- V-T = Exchange of energy between a translationally excited and vibrationally excited molecule.
- rec = Recombination processes.

A few assumptions can be made to simplify the analysis. First, since the dissociation of nitrogen molecules is relatively small at around 2 eV, the average electron energy in the discharge, this term will be small for the ground state (~ 5 %) and zero for the upper states allowing us to neglect this term.<sup>29</sup> We also neglect recombination process, reducing Eq. (21) to,

$$\frac{dN_v}{dt} = \left(\frac{dN_v}{dt}\right)_{e-v} + \left(\frac{dN_v}{dt}\right)_{v-v} + \left(\frac{dN_v}{dt}\right)_{v-T} \quad (22)$$

From the current density, we may approximate the number of electrons in the discharge,  $n_e = J / v_d e$ , where  $J$  is the current density ( $0.047 \text{ A/cm}^2$ ),  $v_d$  is the electron drift velocity in nitrogen ( $\sim 5.5 \times 10^5 \text{ cm/s}$ )<sup>33</sup> and  $e$  is the electron charge ( $1.6 \times 10^{-19} \text{ C}$ ), giving approximately  $5.34 \times 10^{10} \text{ electrons/cm}^3$ . In Figure 39 we can see that the height of the first hot band, and thus the amount of excitation to the first excited state, changed very little throughout the discharge while the height of the ground state, and thus the ground state

number density, changes drastically in the radial direction. This implies some mechanism occurring on axis which is pumping molecules in the ground state to the higher vibrational states. A reasonable assumption is that of excitation to the first excited state by electron impact. Given this, an order of magnitude approximation of the e-V rate, at the average electron energy rather than for the entire electron energy distribution which would require solving the Boltzmann equation, of the system is given by,<sup>34</sup>

$$\left( \frac{dN_{v=1}}{dt} \right)_{e-v} = R_{e-v} N_0 n_e \quad (23)$$

Where,

- $R_{e-v}$  = Rate constant for vibrational excitation due to electron impact.
- =  $2.7 \times 10^{-9} \text{ cm}^3 \text{ sec}^{-1}$  at  $2.0 \text{ eV}^{29}$
- $N_0$  = Molecular density in the ground state,  $3.5 \times 10^{17} \text{ cm}^{-3}$  at 400K.
- $n_e$  = Electron density in the discharge, given above.

This gives a rate of  $5 \times 10^{19} \text{ cm}^{-3} \text{ sec}^{-1}$ . The actual rate for electron impact excitation will undoubtedly be much higher than this rate, however, since in general, the e-V process is closely coupled to the Boltzmann equation for electron distribution function,<sup>32</sup>

$$\frac{\partial n}{\partial t} = -\frac{\partial J_x}{\partial \epsilon} - \frac{\partial J_{ex}}{\partial \epsilon} + \frac{\partial J_{in}}{\partial \epsilon} + \frac{\partial J_{sub}}{\partial \epsilon} + \frac{\partial J_{out}}{\partial \epsilon} \quad (24)$$

Where,

- $n(\epsilon, t) d\epsilon$  = Number of electrons with energy  $\epsilon$ .
- =  $\left( \frac{4\pi}{m_e} \right) \sqrt{\left( \frac{2}{m_e} \right)} \sqrt{\epsilon} f(\epsilon, t) d\epsilon$  (25)
- $m_e$  = Electron mass.
- $f(\epsilon, t)$  = Electron energy distribution function.
- $\epsilon$  = Electron energy, in eV.

$$\frac{\partial J_e}{\partial \epsilon} = \text{Flux of electrons along the energy axis driven by the applied field.}$$

$$\frac{\partial J_{el}}{\partial \epsilon} = \text{Flux of electrons due to elastic collisions.}$$

$$\frac{\partial J_{in}}{\partial \epsilon} = \text{Flux due to inelastic collisions.}$$

$$\frac{\partial J_{sup}}{\partial \epsilon} = \text{Flux due to superelastic collisions.}$$

$$\frac{\partial J_{rot}}{\partial \epsilon} = \text{Flux due to rotational collisions.}$$

This equation gives the number of electrons at a given energy, and both equations must be solved simultaneously to give the actual populations due to electron impact. Clearly, this requires considerable effort and computing power and will not be used as a first approximation. The actual rate calculated may be as high as  $10^{22}$  or  $10^{23} \text{ cm}^{-3} \text{ sec}^{-1}$ , and will be constrained mostly to the center of the discharge where the spatial density of electrons will be at its highest.

The loss due to V-T is given by,<sup>34</sup>

$$\left( \frac{dN_{v=1}}{dt} \right)_{VT} = N_0 N_1 [R_{0 \rightarrow 1} - R_{1 \rightarrow 0}] + N_1 N_2 [R_{2 \rightarrow 1} - R_{1 \rightarrow 2}] \quad (26)$$

$N_0$  = Total number density in the ground state, from data,  $3.5 \times 10^{17} \text{ cm}^{-3}$ .

$N_1$  = Number density in the  $v=1$  state, from data,  $2.5 \times 10^{17} \text{ cm}^{-3}$ .

$R_{a \rightarrow b}$  = Rate constant for transition a to b, in  $\text{cm}^3/\text{sec}$ .<sup>34</sup>

The effects of the V-V interactions are somewhat more complicated than those for V-T because one must now consider both excitation into and out of a given vibrational level. For a cooled discharge, in this case by the nitrogen flow, and for the vibrational temperature much greater than the translational temperature, there will be a preferential direction of exchange of vibrational quanta towards higher vibrational states, that is, from  $v=0$  to  $v=1$ ,  $v=1$  to  $v=2$  and so on. The V-V distribution is also



influenced by the residence time of the molecules in the discharge.<sup>36</sup> As we have already seen from the error in estimation of the gas flow in the two-dimensional study, the residence time can have a dramatic impact on the temperatures of the gas. Under normal conditions in this discharge, 85 sccm, the residence time of molecules in the discharge is on the order of a second. When these factors are multiplied and summed, the V-T rate is  $-6.7 \times 10^{10} \text{ cm}^{-3} \text{ sec}^{-1}$ .

Table 6 gives the rate constants used in both the V-T and the V-V calculations were supplied by Dr. Charles De Joseph of the Aero Propulsion and Power Laboratory at Wright-Patterson Air Force Base in Dayton, Ohio.<sup>34</sup> The higher rate constants for pumping to the higher vibrational levels shows preferential pumping of the higher vibrational levels. This fact is due to the anharmonicity of the nitrogen molecule discussed in Chapter II.

Table 6. Rate constants used in the calculation of V-T and V-V rates.<sup>34</sup>

(all rates given in units of  $\text{cm}^3 \text{ sec}^{-1}$ )

V-T Rates:

$R_{1-0}$	=	$1.364 \times 10^{-22}$
$R_{0-1}$	=	$3.117 \times 10^{-26}$
$R_{1-2}$	=	$9.733 \times 10^{-26}$
$R_{2-1}$	=	$3.838 \times 10^{-22}$

V-V Rates:

$R_{0-1,0}$	=	$4.109 \times 10^{-13}$	$R_{1-0,0}$	=	$4.109 \times 10^{-13}$
$R_{1-2,0}$	=	$6.413 \times 10^{-13}$	$R_{2-1,0}$	=	$7.116 \times 10^{-13}$
$R_{0-1,1}$	=	$7.116 \times 10^{-13}$	$R_{1-0,1}$	=	$6.413 \times 10^{-13}$
$R_{1-2,1}$	=	$1.664 \times 10^{-12}$	$R_{2-1,1}$	=	$1.664 \times 10^{-12}$
$R_{0-1,2}$	=	$8.812 \times 10^{-13}$	$R_{1-0,2}$	=	$7.157 \times 10^{-13}$
$R_{1-2,2}$	=	$2.161 \times 10^{-12}$	$R_{2-1,2}$	=	$1.948 \times 10^{-12}$

The total equation for V-V interaction, with the above factors incorporated, is given by

$$\left( \frac{dN_{v=1}}{dt} \right)_{vv} = N_0 N_1 (R_{0-1,0} - R_{1-0,0} + R_{0-1,1} - R_{1-0,1} + R_{0-1,2} - R_{1-0,2}) + N_1 N_2 (R_{2-1,0} - R_{1-2,0} + R_{2-1,1} - R_{1-2,1} + R_{2-1,2} - R_{1-2,2}) \quad (27)$$

Where,  $R_{a-b,c}$  is the rate constant for a molecule in the vibrational state a to be struck by a molecule in the vibrational state c and, through the gain or loss of energy, left after the collision in the state b. After putting in the correct numbers, the rate for the V-V interaction of a three level system is  $1.4 \times 10^{22} \text{ cm}^{-3} \text{ sec}^{-1}$ .

Substituting the calculated rates for e-V, V-T and V-V into Eq. (22), we have,

$$\frac{dN_V}{dt} = \left( \frac{dN_V}{dt} \right)_{e-V} + \left( \frac{dN_V}{dt} \right)_{V-V} + \left( \frac{dN_V}{dt} \right)_{V-T} = 1.4 \times 10^{22} \text{ cm}^{-3} \text{ sec}^{-1}$$

indicating that the V-V rate dominates the discharge. It should be remembered, however, that the e-V rate has been calculated for only a single electron energy, and as such is severely underestimated. This rate also implies that the population of the first vibrational state should eventually invert. Obviously, since no inversion was observed, there must be other mechanisms which are limiting the population of the vibrational levels. These may include an increase in the loss due to V-T rate for the higher vibrational levels approaching the V-V rates, and shows the inadequacy of this model.<sup>37</sup>

With this data we may now begin to piece together what is actually happening inside the discharge. Assuming a normal distribution of electrons about the center of the discharge, we may conclude that electron-molecule impact will be at its height on axis. Further assuming that the primary vibrational excitation mechanism is that of electron impact in this region, it is not unreasonable to assume that the depopulation of the ground state occurs mainly in this region, with vibrational excitation from V-V interaction enhancing the effect. As these excited molecules begin to drift away from the center of the discharge in a random walk manner, they begin to interact with other molecules. As they drift further from the center of the discharge, the e-V interaction grows weaker and weaker, until the predominant process is now the V-V interaction. V-T interactions will act to slightly depopulate the higher vibrational levels, while the high rate of V-V interaction will tend to take molecules from the lower energy levels and drive

them to higher levels until an equilibrium is reached among the levels. At this point, the V-V interactions have acted to distribute the vibrationally excited molecules throughout the discharge.

This analysis is supported by the general shape of the spectra observed. On axis, the ground state is smallest because the molecules are being pumped to the higher vibrational states by e-V interactions, although, because the diffusion of molecules is a random walk process, some population will be because of V-V interaction. As these molecules drift outward, they begin to randomly distribute their energy throughout the discharge, populating the higher vibrational levels and giving, as seen in this data, a relatively flat profile for the first and second hot bands.

Treanor, *et al.*,<sup>36</sup> found that when the excitation process is dominated by V-V interactions, the vibrational temperature distribution will deviate from the Boltzmann distribution at higher vibrational levels. The Treanor distribution, from Campbell and Muntz,<sup>37</sup> is given by

$$\frac{N_v}{N_0} = \exp \left[ \left( \frac{-vE_1}{k_B \theta_1} \right) + \left( \frac{vE_1 - E_v}{k_B T} \right) \right] \quad (28)$$

Where,

$N_v, E_v$  = Number density and energy of the vibrational level  $v$ , respectively.

$N_0$  = Number density of the  $v = 0$  level.

$v$  = Vibrational quantum number.

$\theta_1$  = The Treanor vibrational temperature given by the relative populations in the  $v = 0$  and  $v = 1$  energy levels.

$T$  = The gas (translational) temperature in Kelvins.

$k_B$  = The Boltzmann constant.

Typical numbers for the difference in the ratio  $N_v/N_0$  for the Treanor to Boltzmann distribution divided by the Boltzmann,  $(\text{Treanor} - \text{Boltzmann})/(\text{Boltzmann})$ , at  $\sim 3$  Torr, 105 mA supply current and a gas temperature of 416 K, from Campbell and Muntz<sup>36</sup> are plotted in Figure 41. At a gas temperature near 500 K, a typical value of the gas temperature in this experiment, the deviation from the Boltzmann distribution is not expected to show up until  $v = 4$  or  $v = 5$ . Obviously, since the measurements taken during this work included only up to  $v = 3$ , deviation was not expected and indeed was not observed. Measurement of the higher order hot bands, however, not permitted by system limitations in the work presented here, should show some deviation.

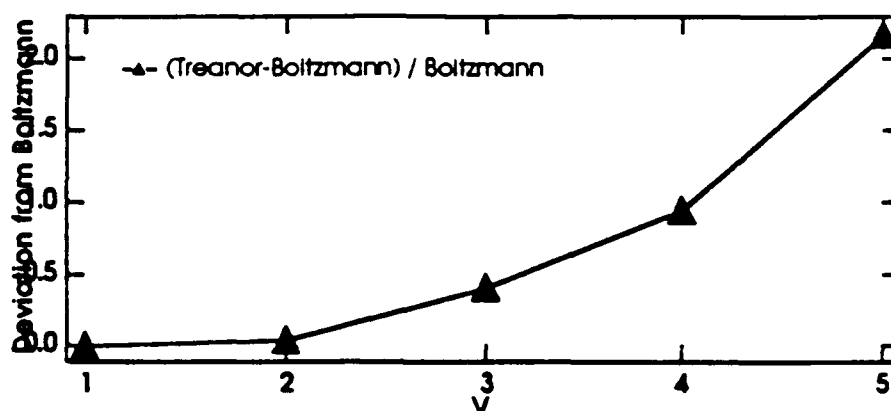


Figure 41. Deviation of Treanor distribution from Boltzmann.<sup>36</sup>

## CHAPTER VI

### CONCLUSIONS AND RECOMMENDATIONS

The work presented here has shown the viability of the CARS system to act as a tool in discharge diagnostics. In this chapter, the results of the experiments will be reviewed and recommendations for the future direction of the project are discussed. These include possible new experiments that could be performed and new discharge geometries that could be looked at by the system in its current mode of operation.

#### Conclusions

##### Dye Laser Evaluation

The evaluation of the Lumonics HyperDye 300 dye laser showed the linewidth to be  $0.07 \text{ cm}^{-1}$ . The linewidth specified by Lumonics in the laser manual was  $<0.05 \text{ cm}^{-1}$  at 607 nm, using  $1 \times 10^{-3}$  molar Rhodamine 590 and a doubled Nd:YAG pump. The extra width observed is possibly due to several factors, the most probable, however, are misalignment of the optics in the laser itself, effects of the dye concentration and possibly the pumping rate by the Nd:YAG pump laser. In the future, these factors should be studied more carefully in order to understand exactly how they affect the shape of the CARS signal. Measurement of the dye laser lineshape should also be carried out using a scanning etalon rather than the OGE effect used here.

##### Discharge Instability

The instability of the discharge in both the chamber voltage and in the CARS signal indicate that the main contributing factors to the formation of an unstable

discharge are the operating current, the cathode cap, the pressure and contaminants in the chamber. It was found that the supply current used by Cirillo, 30 mA, leads to discharge instability both in the visual discharge and in the CARS signal, undoubtedly contributing to the seemingly inconsistent nature of the data taken, and a new operating condition of 20 mA was set. It was also found that the way in which the discharge was struck may lead to instability in the discharge in the form of a hysteresis effect in the chamber voltage.

Because of the uniqueness of this problem, this instability should be studied further in the future. This should include exact measurements of the field inside the discharge as the instability changes from one state to another. The splitting of the positive column can then be quantified in terms of the applied field and of the boundary conditions imposed by the cathode cap and by the nearly wall-less geometry of the system. This information should also prove useful in the new discharge chamber while it is used in a dc glow discharge mode.

### **New CARS Data**

Using the fact that the ground state band in the discharge changes in a parabolic fashion in the radial direction, it was shown that a repeatable and self consistent set of temperature profiles could be obtained using the CARS system. These profiles show that the discharge is relatively flat in terms of the vibrational and rotational temperatures inside the discharge, decreasing gradually with increasing radius with a definite drop outside the discharge region.

Using the relative heights of the first and second hot bands with the height of the ground state band, we have begun to piece together the mechanisms involved with this discharge. The variation of the population of the ground state with radius indicates that the pumping of molecules from the ground state to the first and second vibrational

levels, the only other levels measured in this experiments, is dominated by electron impact induced vibrational excitation and vibrational-vibrational collision excitation. In the simplified analysis of the discharge used here, where only pumping to the first vibrational level is calculated, vibrational - translational collisions act as a depopulation term, but are not large enough to force the system into equilibrium. Therefore, it is believed that the equilibrium is reached through a combination of rates not calculated here, such as dissociation and recombination, and that these rates play a greater role in the discharge than was considered previously. Another possibility is that the V-V rate which dominates the pumping rate to the first vibrational level becomes progressively lower at higher  $v$  until it is small enough to allow the depopulation terms to take over and bring the discharge into equilibrium. At these high V-V rates, the vibrational temperature distribution in the discharge should show signs of a non-Boltzmann behavior and should show signs of a Treanor-like distribution. To see these effects however, the  $v > 4$  bands need to be measured as well.

The two main conclusions to be drawn from the discharge data presented here are the following: 1) The vibrational and rotational temperatures do not change sharply as had been reported by Epling and Cirillo, but are relatively flat throughout the discharge dropping only at the edges indicating that the mechanisms for excitation and de-excitation are relatively well behaved functions of the discharge. 2) Of the excitation mechanisms examined, the V-V rate dominates at the lower values of  $v$  and at higher  $v$  values the discharge should show a Treanor-like distribution.

### **Recommendations**

The first recommendation is to finish the study of the dc discharge as quickly as possible and to move on to a pulsed discharge system. Pulsed discharges are much better behaved than dc discharges and should show the CARS system capable of

making measurements in a simple and straight forward manner.<sup>29</sup> This would entail changing the system very little, the major change coming in two areas, the discharge chamber and the electronics. A new discharge chamber designed by Dr. Yaney and Mr. Don Linder, shown in Appendix A, was been designed to have the capability for pulsed discharge studies. The modifications to the electronics entail the implementation of a new LeCroy 12-channel ADC in place of the Nicolet presently used in the system and the development of the software needed to interface the LeCroy unit to the computer. This process has already begun with the help of Dr. Yaney and Mr. John Parrish, a fellow Electro-Optics student working for Dr. Yaney at the University of Dayton. The system should also allow the monitoring of several parameters of the system. These include the pulse-to-pulse fluctuations from the YAG and dye lasers. This information can then be used to normalize the data to remove some of the background noise and to extend the range of measurable hot bands.

The move to pulsed discharge will be accompanied by a redesigned CARS optical system. This design activity was carried out as part of this thesis work and is described in Appendix A. The new design will be part of a new CARS laboratory in Room D120 of Building 450 at Wright-Patterson AFB. The move to this new lab is expected to be completed by July of 1991.

With the switch to a pulsed discharge, two new pieces of equipment would greatly enhance the data collecting ability of the system by speeding the process: 1) A switch to a linear array detector to replace the photomultiplier tube presently used in the system to help speed the data collection time. 2) The LeCroy ADC needs to be installed and software written which allows more data to be taken in a shorter period of time and greater control over the experiment from the computer.



## REFERENCES

1. P. P. Yaney, 'Experimental Studies and Characterization of Gaseous Electrical Discharge Media Using Coherent Anti-Stokes Raman Spectroscopy (CARS),' Final Report to University Resident Research Program of the Air Force Office of Scientific Research, Bolling Air Force Base, D.C., (1990).
2. C. J. Emmerich, 'Development of a Coherent Anti-Stokes Raman Spectroscopy System for use in Plasma Diagnostics,' Master's thesis for the University of Dayton Electro-Optics Program, (April, 1986).
3. D. D. Hodson, 'Positive-Column Nitrogen Discharge Studies using Coherent Anti Stokes Raman Spectroscopy,' Master's thesis for the University of Dayton Electro-Optics Program, (April, 1987).
4. J. E. Oleksy, 'Development of a Coherent Anti-Stokes Raman Spectroscopy System for Studies of Gaseous Discharge Media,' Master's thesis for the University of Dayton Electro-Optics Program, (August, 1988).
5. B. L. Epling, 'Spatially Resolved Temperature Studies in  $N_2$  and  $N_2$  - Ar Discharges using Coherent Anti-Stokes Raman Spectroscopy,' Master's thesis for the University of Dayton Electro-Optics Program, (July, 1989).

6. J. Cirillo, "Development of a High-Resolution Coherent Anti-Stokes Raman Spectroscopy System for use in the Study of Electrical Discharges in  $N_2$ ," Masters thesis for the University of Dayton Electro-Optics Program, (July, 1990).
7. C. V. Raman and K. S. Krishnan, "A Change of Wavelength in Light Scattering," *Nature*, **121** (1928).
8. P. D. Maker and R. W. Terhune, "Study of Optical Effects Due to an Induced Polarization Third Order in the Electric Field Strength," *Physical Review*, **137**, 801 A, (1965); R.W Terhune, invited Speaker, *Am. Phys. Soc.* **8**, 359 (1963).
9. P. R. Regnier and J. P. E. Taran, "On the Possibility of Measuring Gas Concentrations by Stimulated Anti-Stokes Scattering," *Appl. Phys. Letts.* **23**, 240-242 (1973).
10. S. Druet, B. Attal, and J. P. E. Taran, "Electronic Resonance Enhancement of Coherent Anti-Stokes Raman Scattering," *Phys. Rev. A* **18**, 1529-1557 (1978).
11. A. C. Eckbreth, Laser Diagnostics for Combustion Temperature and Species, (Abacus Press, Cambridge, Mass., 1988).
12. J. W. Nibler, "Coherent Anti-Stokes Raman Spectroscopy," in Raman Spectroscopy of Gases and Liquids, A. Weber, Editor (Springer-Verlag, New York, 1979), Chapter 7.
13. A. C. Eckbreth, "BOXCARS : Crossed-Beam Phase-Matched Cars Generation in Gasses," *Appl. Phys. Lett.* **32**, 7 (1978).

14. G. Herzberg, Molecular Spectra and Molecular Structure, Vol I Spectra of Diatomic Molecules, (D. Von Nostrand Company, Inc., New York, 1950).
15. A. Lofthus and P. H. Krupenie, "The Spectrum of Molecular Nitrogen," J. of Phys. and Chem. Ref. Data **6**, 1 (1977).
16. J. T. Verdeyen, Laser Electronics, Second Edition (Prentice Hall, Englewood Cliffs, N.J., 1989), Chapter 15.
17. T. Dreier, U. Wellhausen and J. Wolfrum, "CARS Studies of Vibrationally Excited Nitrogen at Low Pressures," Appl. Phys. B, 31-36. (1982).
18. W. M. Shaub, J. W. Nibler and A. B. Harvey, "Direct Determination of Non-Boltzmann Vibrational Level Populations in Electric Discharges by CARS," J. Chem. Phys. **5**, 1883-1886 (1977).
19. B. Massabieaux, G. Gousset, M. Lefebvre and M. Pealat, "Determination of  $N_2(X)$  Vibrational Level Populations and Rotational Temperatures using CARS in a DC Low Pressure Discharge," J. Physique **48**, 1939-1949 (1987).
20. M. Pealat, J. P. E. Taran and J. Taillet, "Measurement of Vibrational Populations in Low-Pressure Hydrogen Plasma by Coherent Anti-Stokes Raman Scattering," J. Appl. Phys. **52** (1981).
21. B. Barbieri, N. Beverini and A. Sasso, "Optogalvanic Spectroscopy," Rev. of

Mod. Phys. **62**, 603-644 (1970).

22. R. Keller, R. Engleman and E. Zalewski, "Opto-galvanic Spectroscopy in a Uranium Hollow Cathode Discharge," J. Opt. Soc. Am. **69**, 738 (1979).
23. R. Keller and E. Zalewski, "Optogalvanic Responce to Light: Photon Energy vs. Photon Number; Comments," Appl. Opt. **21**, 3992 (1982).
24. R. Keller, B. Warner and E. Zalewski, J. Phys. (Paris) **C7-44**, 23 (1983).
25. M. Broglia, F. Catoni, A. Montone and P. Zampetti, "Galvanic Detection of Laser Photoionizatoion in Hollow Cathode Discharges: Experimental and Theoretical," Phys. Rev. A **36**, 705 (1987).
26. A. Yariv, Quantum Electronics, Third Edition, (John Wiley & Sons, Inc., NY, 1989), Chapter 8.
27. P. P. Yaney, M. Millard and J. Cirillo, "Studies of Temperature Profiles of N<sub>2</sub> in a DC Glow Discharge using High Resolution CARS," Contributed Paper, 43rd Annual Gaseous Electronics Confrence of the American Physical Society, Champaign-Urban, Illinois, October 16 - 19, 1990, Bull. Am. Phys. Soc. **36**, 216 (1991).
28. M. Millard and P. P. Yaney, "Measurement of Instability in a N<sub>2</sub> Normal Glow Discharge Using CARS," Contributed Paper, Dayton Cincinnati Section of the AIAA, 17th Annual Mini Symposium on Areospace Science and Technology, Dayton, Ohio, March 14th, 1991.

29. A. Garscadden, (Private Communications), Aero Propulsion and Power Laboratory, Wright-Patterson Air Force Base, Dayton, Ohio, (1990-1991).
30. P. P. Yaney and M. W. Millard, "Studies of Nonequilibrium Profiles in Wall-Less  $N_2$  Gaseous DC Discharge Using Scanning BOXCARS," Contributed Paper, 1990 Joint Conference on Lasers and Electro-Optics and Quantum Electronics and Laser Science, Baltimore, Maryland, May 11 - 17, 1991.
31. M. Millard and P. P. Yaney, "Vibrational and Rotational Temperature Measurements in a  $N_2$  Normal Glow Discharge," Contributed Paper, Ohio Section of the American Physical Society Meeting, Ohio University, Athens, Ohio (1991).
32. M. Capitelli M. Dilonardo and C. Gorse, "Coupled Solutions of the Collisional Boltzmann Equation for Electrons and the Heavy Particle Master Equation in Nitrogen," Chem. Phys., 56, 29-42 (1981).
33. L. Huxley and R. Crompton, The Diffusion and Drift of Electrons in Gases, (John Wiley & Sons, Inc., NY, 1974).
34. C. DeJoseph, (Private Communications), Aero Propulsion and Power Laboratory, Wright-Patterson Air Force Base, Dayton, Ohio, (1991).
35. G. E. Caledonia, S. J. Davis, B. D. Green, L. G. Piper, W. T. Rawlins, G. A. Simons and G. M. Weyl, "Analysis of Metastable State Production and Energy Transfer," Air Force Publication, AFWAL-TR-86-2078, Aero Propulsion Laboratory, Wright

Patterson Air Force Base, Dayton, Ohio, (1986).

36. C. E. Treanor , J. W. Rich and R. G. Rehm, "Vibrational Relaxation of Anharmonic Oscillators with Exchange Dominated Collisions," J. Chem. Phys., 48(4), 1798 (1968).
37. D. H. Campbell and E. P. Muntz, "Non-Boltzmann, Non-Treanor Vibrational Level Populations of Electrical Discharge Excited Nitrogen," J. Chem. Phys., 72(3), 1487 (1980).

## **APPENDIX A**

### **New CARS Optical System**

At the conclusion of this thesis activity, the CARS optical system will be moved to a new location in room D120 of Building 450 at Wright-Patterson AFB. This move provided an opportune time to optimize the system. The new experimental design, shown in Figure A1, is intended to simplify the optics of the system considerably by removing as many unnecessary components as possible and arranging what was left into a simpler system. In part, this was accomplished by removing the separate optical delay lines formerly used to equalize the path lengths of the pump and probe beams. This allowed the removal of the mirrors M2 and M3, beam splitter BS2 and prisms P4, P5 and P6, in Figure A1, needed to redirect the pump beams. Instead, the Nd:YAG beam is split at the latest possible point before entering the focusing lens by use of the vertical beam splitter labeled Beam Splitter. Here, the beam is split into two beams approximately 3 cm apart by a single beam splitter (BS2) and a mirror (M1), as shown in Figure A2. Separating the pump beams in this way introduces a timing difference of 0.1 ns between the two pump beam pulses. The delay line in this case may also be varied easily by moving prisms P3 and P4 until the pulse from the dye laser and the pump lasers match as closely as possible.

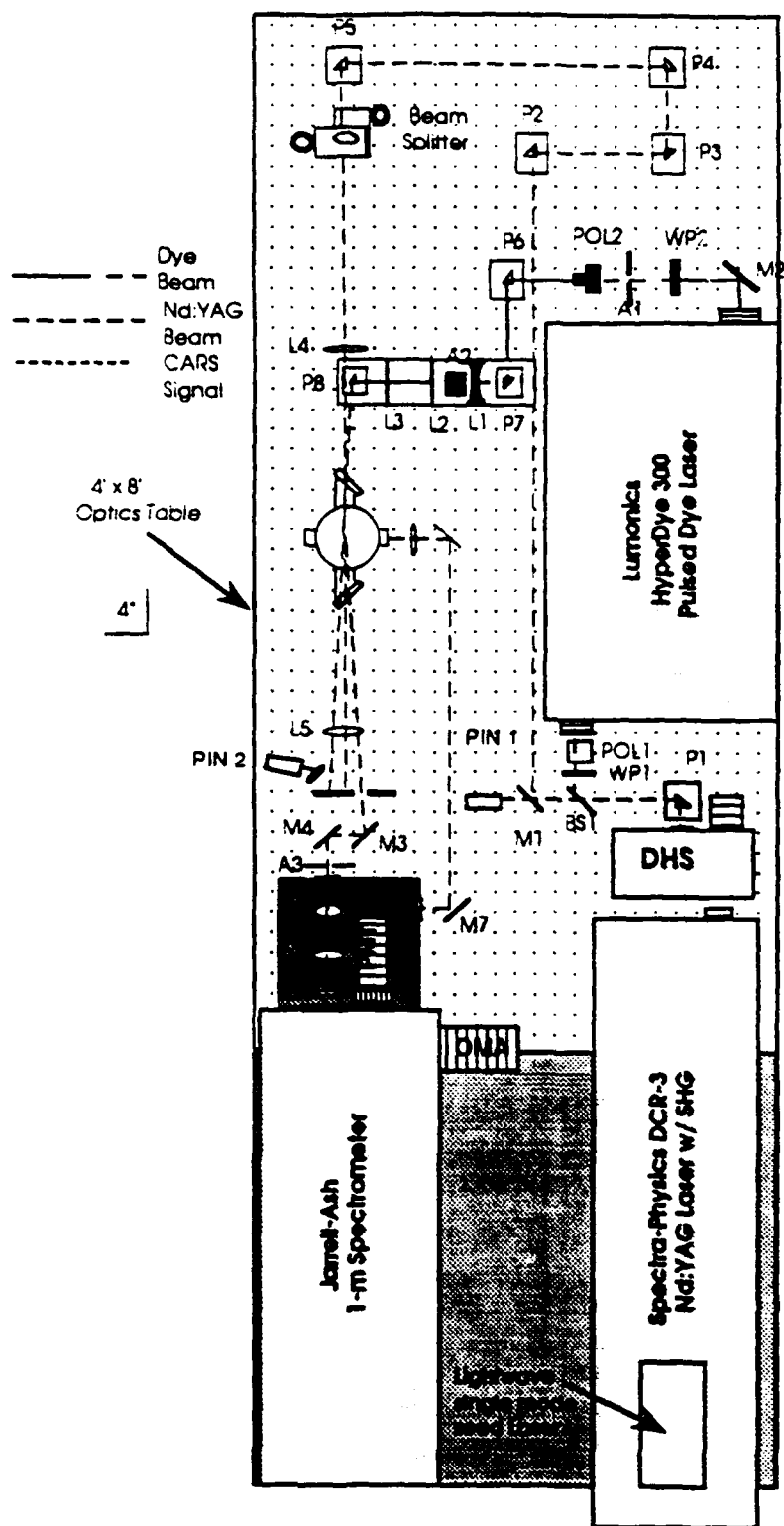


Figure A1. Layout of the new CARS optical system to be implemented in July of 1991.



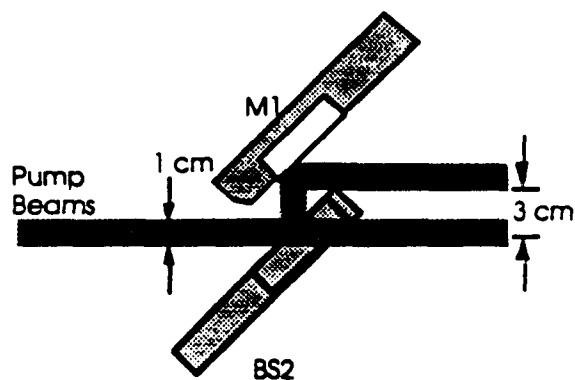


Figure A2. Beam splitter of Figure A1.

In the old CARS system, Figure 9, the spectrometer was rotated so that the entrance slit to the spectrometer was facing away from the discharge chamber. This was a holdover from the time when the system was in the colinear CARS setup. In the new system, the spectrometer has been arranged to allow the CARS beam to feed directly into the spectrometer with a minimum of optics and also to allow the spectrometer to be used in the scanning mode for normal emission spectroscopy. The new arrangement is illustrated in Figure A3. The box surrounding the spectrometer entrance and photomultiplier is a light tight box with removable panels that allow direct access to the front panel of the spectrometer with a minimum of effort.

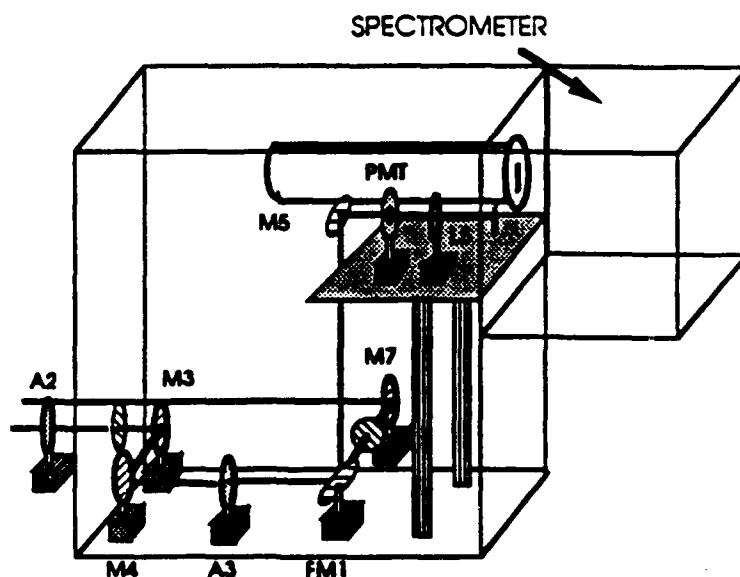


Figure A3. Entrance to the spectrometer in the new CARS system.

The new system also has a new chamber, designed and built by Dr. Yaney and Mr. Don Linder, a schematic of which is given in Figure A4. The new chamber has the advantage of allowing the electrodes to be removed without the necessity of taking the whole chamber apart as was the case with the older system. In addition to this feature, the new chamber has larger windows at the entrance and exit ports allowing for a greater range of movement of the control volume inside the discharge. The chamber was also positioned at a point on the optics table where a switch to longer focal length lenses at a later date can easily be incorporated into the system by expanding on either side of the chamber rather than moving it.

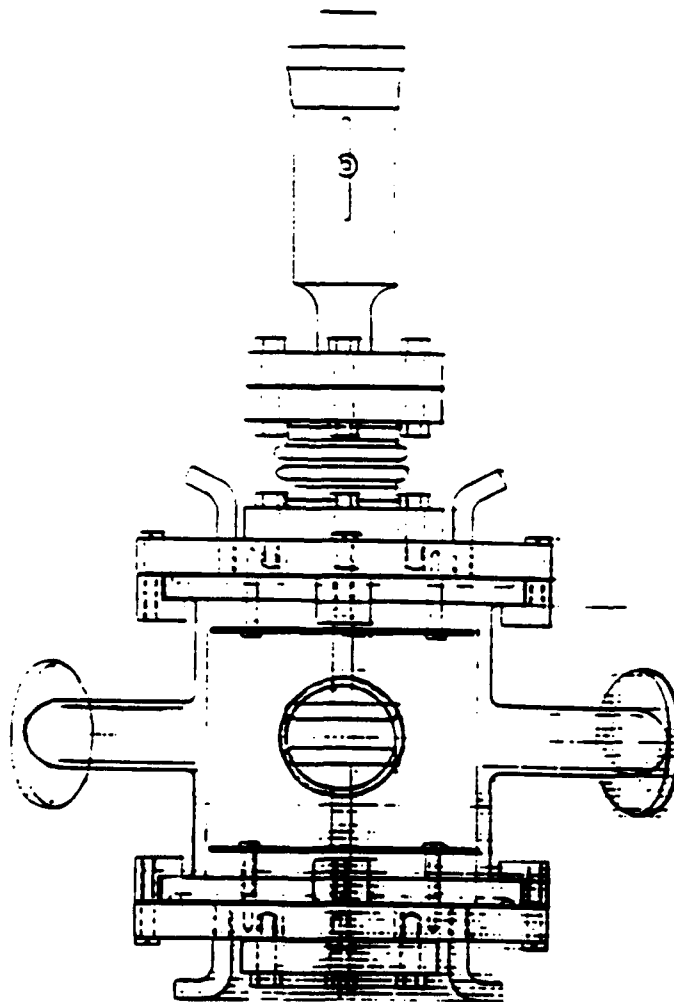


Figure A4. Schematic diagram of the new discharge chamber.